Nanoscale electron tomography and compositional analysis of Aerotaxy nanowires

Persson, Axel

2018

Document Version:
Publisher's PDF, also known as Version of record

Nanoscale electron tomography and compositional analysis of Aerotaxy nanowires

CENTRE FOR ANALYSIS AND SYNTHESIS | LUND UNIVERSITY
AXEL PERSSON

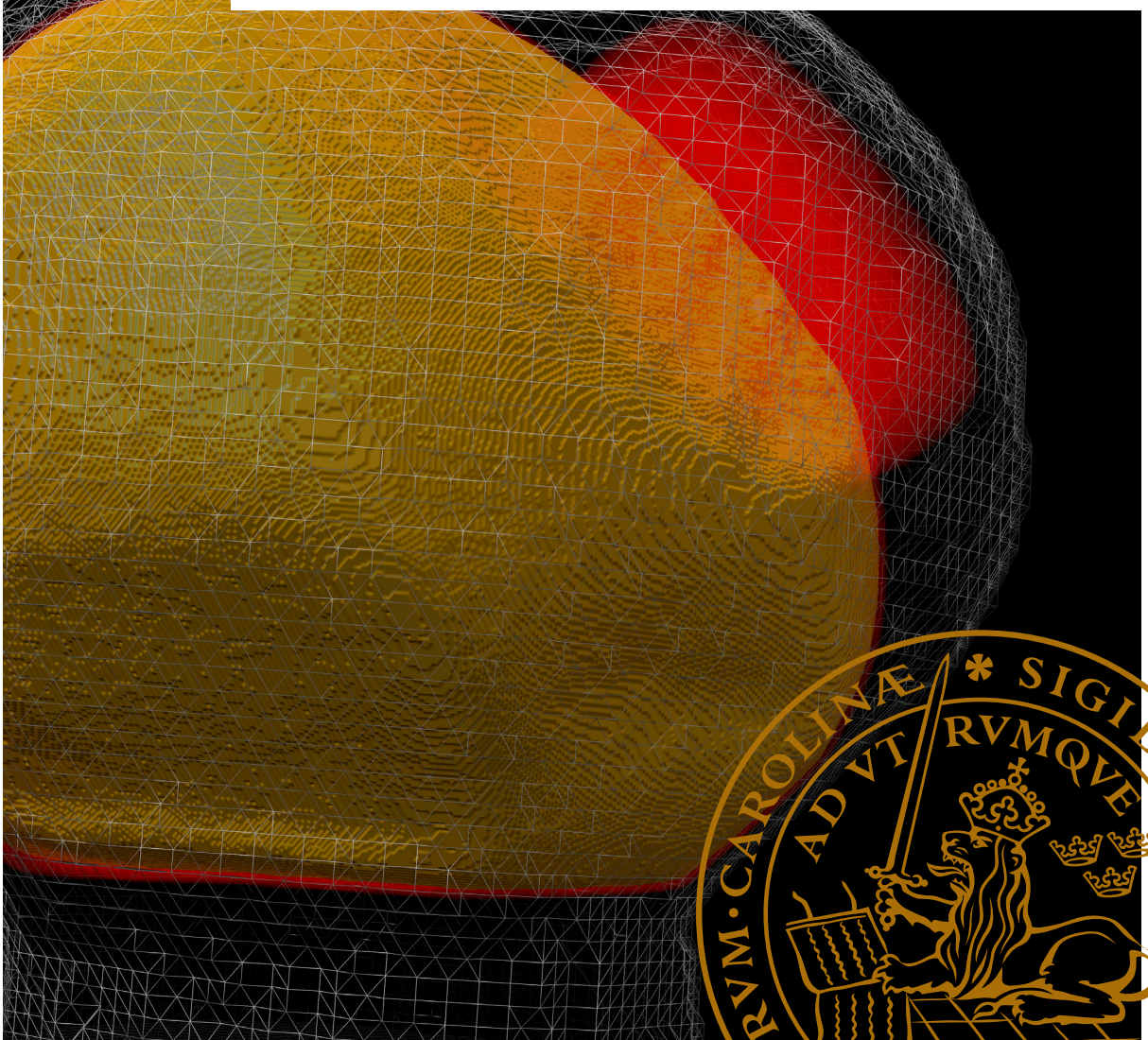

Nanoscale electron tomography and compositional analysis of Aerotaxy nanowires

Nanoscale electron tomography and compositional analysis of Aerotaxy nanowires

by Axel Persson

LUND
UNIVERSITY

Thesis for the degree of Licentiate
Thesis advisors: Professor Reine Wallenberg,
Associate Professor Martin Magnusson
Faculty opponent: Dr. Tom Willhammar, Stockholm University

To be presented at Kemicentrum Department of Chemistry, lecture hall G
on Friday, the 16th of March 2018 at 13:15.

Organization	Document name
LUND UNIVERSITY Department of Chemistry Box 124 SE–221 00 LUND Sweden	**LICENTIATE DISSERTATION** Date 2018-03-16 Sponsoring organization
Author(s) Axel Persson	

Title (and subtitle)

Nanoscale electron tomography and compositional analysis of Aerotaxy nanowires

Abstract

One common goal of sample analysis is to provide structural, compositional, or functional data in order to improve production parameters. One instrument specialized in such structural and compositional analysis with a high spatial resolution is the transmission electron microscope (TEM). The high-end microscopes have the capability of sub-Ångström resolution and compositional quantification and distribution, which makes it the instrument of choice for many different research fields. For example, the composition, crystallography, and overall morphology of semiconductor nanowires is highly dependent of the multi-parameters space of the growth, and needs the high resolution analysis and imaging.

Here we present the use of TEM for structural, compositional and morphological analysis of semiconducting nanowires grown by Aerotaxy, which is a technique for growing nanowires without the need for an expensive single crystalline substrate. This, in combination with it being continuous holds high hopes for industrial application of nanowires in the future. The TEM analysis provides high resolution micrographs of the single crystalline nanowires for growth quality evaluation, as well as compositional analysis, whereas electron tomography (ET) is used to determine the general morphology of the nanowires by reconstructing 3D images of the wires. The 3D data is especially used for surface features, and provides data for topological surface maps of the wire, which we have named azimuthal maps. Hopefully the data can provide more insight in the growth mechanism of Aerotaxy making highly controlled growth possible.

Key words

Transmission electron microscopy, Electron tomography, Nanowires, Aerotaxy

Classification system and/or index terms (if any)

Supplementary bibliographical information	Language
	English
ISSN and key title	ISBN
	978-91-7422-571-6 (print) 978-91-7422-572-3 (pdf)
Recipient's notes	Number of pages: 111 / Price
	Security classification

Nanoscale electron tomography and compositional analysis of Aerotaxy nanowires

by Axel Persson

LUND
UNIVERSITY

A licentiate thesis at a university in Sweden takes either the form of a single, cohesive research study (monograph) or a summary of research papers (compilation thesis), which the doctoral student has written alone or together with one or several other author(s).

In the latter case the thesis consists of two parts. An introductory text puts the research work into context and summarizes the main points of the papers. Then, the research publications themselves are reproduced, together with a description of the individual contributions of the authors. The research papers may either have been already published or are manuscripts at various stages (in press, submitted, or in draft).

Cover illustration front: A tomographic reconstruction of a nanowire seed particle on top of the nanowire (Sn-doped GaAs) grown by Aerotaxy. The particle have segregated into different phases, which are segmented with colors. The yellow volume is a line phase of Ga_2Au, the red volume is a Sn-rich phase, while the rest is the Ga-rich phase. The wire is part of the study in paper III.

Cover illustration back: HRTEM image of some droplets on a nanowire surface. One of these have nucleated growth of a branch. The wire is part of the study in paper III.

Funding information: The thesis work was financially supported by Knut and Alice Wallenberg foundation (KAW), Energimyndigheten and NanoLund.

Faculty of Engineering, Department of Chemistry

ISBN: 978-91-7422-571-6 (print)
ISBN: 978-91-7422-572-3 (pdf)

Printed in Sweden by Media-Tryck, Lund University, Lund 2018

"In a dark place we find ourselves, and a little more knowledge lights our way"
Star Wars Episode III: Revenge of the Sith

"Your eyes can deceive you; don't trust them"
Star Wars Episode IV: A New Hope

Acknowledgements

There are many people to thank for enabling me to do research and experiencing such an interesting international workplace.

With the standard conversation: "– Am I disturbing? – Yes... come on in (cue half an hour of discussion)", I would like to thank my supervisor Reine for all input and advice. I do not know how you could have such confidence in me using the expensive electron microscopes from the first days of summer-SEM to the newly arrived cryo- and E-TEMs, but I'm very thankful for the opportunity. Also, I would like to thank my co-supervisor Martin for bringing additional views to our group and constantly having projects going. I am looking forward to see what the coming years will offer with you two as my supervisors.

With advanced equipment comes a lot of things to handle and I am grateful to have such a competent crew keeping me and the microscopes in check. Thank you Anna, Crispin, and Daniel for doing the work in the background and fixing problems, as well as discussing ideas. Thank you also Gunnel.

Lacking fellow PhD students in my own group, I would like to reach out across the campus to people, involved in the microscopy, especially Filip, Marcus and Carina. Marcus and Carina, you better beware of me joining you at Dagobah. A force of science to be reckoned with, we will be.

Thank you Polymat and *Dr. Nano* for the coffee, lunch and what-not-discussions about everything. Laura, we need to stand our ground against the ever growing group of polymer people.

In order to stay sane during intense weeks of research, especially during writing, I am glad that I have my trumpet. I would like to thank the people of the orchestra HvMk Eslöv by, probably being one of the first i world history to, in a thesis, include:

Heja ESLÖV!

Thanks also to my family and especially Emma, without whom nothing would be possible.

Contents

List of publications

This thesis is based on the following publications, referred to by their roman numerals:

I **Electron tomography reveals the droplet covered surface structure of nanowires grown by Aerotaxy**

Axel R. Persson, Wondwosen Metaferia, Sudhakar Sivakumar, Lars Samuelson, Martin H. Magnusson, L. Reine Wallenberg
Manuscript

II **GaAsP Nanowires Grown by Aerotaxy**

Wondwosen Metaferia, **Axel R. Persson**, Kilian Mergenthaler, Fangfang Yang, Wei Zhang, Arkady Yartsev, Reine Wallenberg, Mats-Erik Pistol, Knut Deppert, Lars Samuelson, Martin H. Magnusson
Nano Letters **16** (2016) 5701, ACS AuthorChoice - Open Access

III **n-type doping and morphology of GaAs nanowires in Aerotaxy**

Wondwosen Metaferia, Sudhakar Sivakumar, **Axel R. Persson**, Irene Geijselaers, Reine Wallenberg, Knut Deppert, Lars Samuelson, and Martin H. Magnusson
Submitted 2018

Publications which I contributed to but are outside the scope and not included in this thesis:

Individual Defects in InAs/InGaAsSb/GaSb Nanowire Tunnel Field-Effect Transistors Operating below 60 mV/decade

Elvedin Memisevic, Markus Hellenbrand, Erik Lind, **Axel R Persson**, Saurabh Sant, Andreas Schenk, Johannes Svensson, Reine Wallenberg, Lars-Erik Wernersson
NanoLetters **17** (2017) 4373

Vertical InAs/InGaAs Heterostructure Metal–Oxide–Semiconductor Field-Effect Transistors on Si

Olli-Pekka Kilpi, Johannes Svensson, Jun Wu, **Axel R Persson**, Reine Wallenberg, Erik Lind, Lars-Erik Wernersson
Nano Letters **17** (2017) 6006

Polymer-supported palladium (II) carbene complexes: catalytic activity, recyclability and selectivity in C-H acetoxylation of arenes

Maitham H Majeed, Payam Shayesteh, Reine Wallenberg, **Axel R Persson**, Niclas Johansson, Lei Ye, Joachim Schnadt, Ola F Wendt
Chemistry-A European Journal **23** (2017) 8457

Popular summary in English

It is probably not necessary to state the scientific importance of microscopy. Microscopes make observations possible of objects that otherwise would not be visible. Such an analysis can tell us about the nature of an object, and perhaps how and why it functions as it does. Application of microscopy is broad and can be used for analyzing anything from biological structures, small particles, minerals, to the modern materials of today.

Through electron microscopy the limit for what is possible to see has been moved. The resolution can be better than an Ångström, a tenth of a billionth of a meter, which makes it possible to see atomic arrangements. This is actually necessary for materials science since it nowadays has the capability of manipulation on the atomic scale. Atomic control can create improvement, such as: higher strength, less weight, higher electrical conductivity, more intense light emission, or stronger magnetic activity, in a wide range of materials. Combining different elements and structures will lead the way for the development of materials science and it is hence important to analyze the results of different production procedures in an exact way, something made possible by electron microscopy.

My research deals with the usage of transmission electron microscopy (TEM) and how to use it for analysis of small structures, called nanowires. TEM is a kind of electron microscope where electrons are transmitted through a sample and then detected on the other side. This will create an image of the sample, which can be greatly magnified. Using the TEM it is possible to image the atomic structure of the nanowires, which are thin (between 10 and 200 nanometers), and determine which elements are present and the crystal quality of structure. This is important since the analysis will help in giving guidance on how to produce as good nanowires as possible. The idea is to use the nanowires as transistors, LEDs, or perhaps solar cells in the future.

One additional analysis, which I have used in this thesis, is electron tomography. Tomography is the same techniques as physicians use at the hospital, in what is known as a CT scanner. In this technique an X-ray machine records many images through a patient at different angles, and then it is all put together to form a 3D image, making it unnecessary to cut open the body. I have used the same principle but with electrons in the TEM and by that created 3D images of the nanowires. This is a very useful tool for analyzing the whole volume and its surface structures which in turn can be very important for the behavior of the material.

Populärvetenskaplig sammanfattning på svenska

Att mikroskop har varit användbara för vetenskapen kan nog många hålla med om och också lätt förstå. Observationer av det som finns runt omkring oss gör att vi kan förstå hur saker fungerar, hänger ihop och passar in. Mikroskop kan i allmänhet hjälpa det mänskliga ögat att se det som annars inte är möjligt, vilket är avgörande då man vill förstå bland annat små biologiska strukturer, partiklar, mineraler, eller moderna material.

Genom utvecklingen av elektronmikroskopi har möjligheterna ökat än mer och punkt-till-punkt-upplösningen är numera bättre än en Ångström, en tiondels miljarddel av en meter, vilket gör att man lätt kan observera atomers positioner. Atomer som är organiserade i någon form av kristall, så som i en metall, har ett avstånd sinsemellan på några Ångström och tackvare att man nu kan se dessa kan man också förstå hur dessa sitter ihop och koppla fenomen till hur atomerna är arrangerade. Det är på denna nivå som materialvetenskapen befinner sig på för tillfället: hur man kombinerar olika ämnen på atomnivå för att tillverka starka, lätta, elektriskt ledande, lysande eller magnetiska material på bäst sätt. Dessa egenskaper bestäms och kan även manipuleras på atomnivå vilket gör att det också är viktigt att använda elektronmikroskopin för att analysera resultat av tillverkningen och kanske jämföra med väl fungerande material i naturen.

Min forskning handlar om att använda transmissionselektronmikroskopi (TEM) för att analysera olika typer av material, i denna avhandling främst halvledande nanotrådar. I ett TEM skickar man elektroner genom sitt prov och detekterar dessa på andra sidan, vilket alltså kan skapa mycket högupplösta bilder. Proverna, nanotrådarna, kan vara mellan 10 och 200 nanometer tjocka och är tänkta att kunna användas som elektroniska komponenter, kanske transistorer, lysdioder eller solceller. För att fungera på bästa sätt behöver man hitta tillverkningssätt som skapar så perfekta trådar som möjligt. Genom att analysera atomernas arrangemang samt även se vilka typer av atomer som finns närvarande har jag hjälpt koppla sätt att tillverka trådarna på till det faktiska resultatet.

Ytterligare ett sätt att analysera proverna på, vilket jag börjat använda på nanotrådar men som även har annan potential, kallas elektrontomografi. Tomografi är samma teknik som man använder på sjukhus när man skickar en patient genom en maskin, sk skiktröntgen, som tar bilder från olika vinklar runt hela kroppen och återskapar en 3D modell för läkaren. Genom att utföra samma process i ett TEM, tomografi med hjälp av elektroner, kan man återskapa mycket små objekt i 3D. Detta kan vara essentiellt för att analysera ytstrukturer och volymer, vilka i sin tur också kan påverka ett materials egenskaper.

Chapter 1

Introduction

In most research, analysis is of great importance in order to verify and evaluate synthesis or industrial large scale production. Structural and compositional analysis are both naturally the analysis of choice when the properties of the sample or product greatly depend on these properties. Materials science is one such example of research, where properties of different elements are combined in order to realize improved properties. Not only the composition, but the structure, shape, and surface properties can completely change the way a material behaves, mechanically, optically, electrically or magnetically [1, pp. 1-18]. Hence the importance to evaluate the synthesis.

The reasons for materials science research could be to combine cheaper components in order to replace an expensive and/or rare material. Additionally, a material might achieve superior properties if it is produced with a certain crystal structure or surface chemistry. Materials science has been developed to the point that properties are altered on the atomic scale, which means that analysis is also required on the same spatial level. Examples of instruments capable of that kind of analysis are electron microscopes, with the two main types being scanning and transmission electron microscopes (SEM and TEM), which both are capable of high spatial resolution and compositional analysis [2, p. 5].

In this thesis, transmission electron microscopy techniques are described with the focus on analyzing a certain class of materials called III–V semiconductor nanowires due to the materials combination of elements from group III (Al, Ga, In) and group V (N, P, As, Sb) in the periodic table. The III–V materials used have the shape of thin wires with the dimensions of a couple of tens of nm in diameter and generally around one to a couple of µm in length. The small size requires the use of transmission electron microscopy for determination of local properties, such as compositional changes

or lattice structure. The transmission electron microscope is described in chapter 3 where modes of operation and concepts are presented, especially for the use on III–V semiconductor nanowires.

Chapter 2 describes the basics of nanowire growth and how the different properties can form through adjustment of growth conditions. Also, the special form of aerosol-based nanowire growth, Aerotaxy, is presented in section 2.3. The nanowires analyzed for this thesis are all produced using this method and the TEM analysis could hopefully help in understanding it better.

While transmission electron microscopy has lots of advantages, there are some limitations due to the projection of the sample. One of these is retrieval of spatial information in all directions. One technique, or rather an additional mode of operation for the microscope, is presented in chapter 4, namely tomography. Tomography as a technique is not new, but its usage in highly resolving electron microscopy is more recent, and the application in nanowire research is presented in that chapter.

1.1 Why nanowires?

Semiconductor research is a hot topic due to its application in modern electronics [3–5], and what makes semiconductors so cost efficient is the abundance of the most commonly used raw-material: silicon [6]. Silicon is such a cheap material that proposed alternative materials cannot be expected to easily replace it but rather offer complementary solutions [7]. III–V semiconductors are, as mentioned, a combination of materials from groups adjacent to silicon, which make them semiconducting just as silicon, while other properties are tunable by the relative composition of the components [7]. This offers a complement to the silicon and can be used in specialized electronic components to increase their efficiency [7]. However, producing electronic components often involves combining regions of different properties, known as heterostructures. The properties are, for example, band gap and lattice parameter, and that poses a practical problem since crystals of different lattice parameters are difficult to combine.

Mismatch between two lattices results in large strain at the interface between the crystals, which can cause dislocations and defects, which can drastically impede the performance [8]. However, nanowires have the ability to relax strain to a higher degree which makes it possible to combine heterostructures not possible in bulk [9, 10]. One additional feature of III–V nanowires in contrast to bulk is a controllable polymorphism [11]. This means that grown nanowires can have a different crystal structure than the thermodynamically stable one that occurs in bulk, and this further adds to

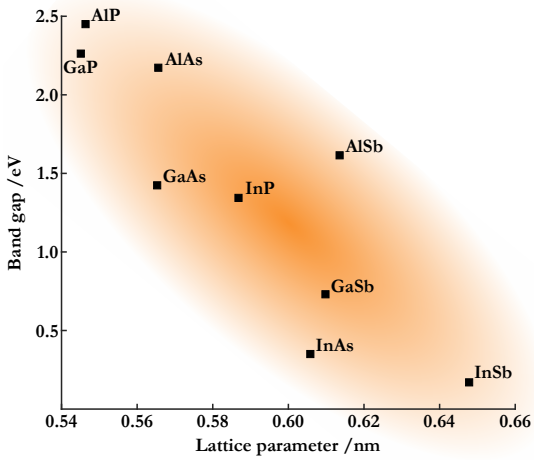

Figure 1.1: A map over lattice parameters and band gaps for combinations of III–V materials. The binary combinations are marked with their name, and points in between can be achieved by adding more elements [7].

the multiple possibilities with nanowires since different crystal structures of the same material have different properties.

1.2 An introduction to electron microscopy

The reason for using *electron microscopy* (EM) instead of *visual light microscopy* (VLM) is the advantage in spatial resolution. Using electrons accelerated towards the sample, it is possible to observe objects significantly smaller than the limits of VLM. This makes EM a very important instrument for material science, but also biological applications for observing cells or proteins are possible [12, 13]. With the same principle as glass or plastic lenses for VLM, EM uses electromagnetic lenses capable of deflecting the charged electrons despite their high velocities. This makes it possible to focus the electrons to form an image and alter both magnification and focus.

While scanning electron microscopy (SEM) uses a focused probe to raster across the surface of a thicker sample, and mainly analyzes secondary electrons *emitted* from the surface, this thesis is focused on the usage of transmission electron microscopy (TEM) which instead uses higher energy electrons that are transmitted through a thin sample and collected on the other side.

The TEM has the capability to resolve atomic structures as long as the sample permits high transmission [2, pp. 5-6]. Luckily the samples analyzed for this thesis are nanowires, which are thin enough as synthesized. Otherwise, extensive sample preparation

is usually needed in order to make them thin enough for the TEM. This can be done by thinning through polishing or cutting thin slices of the sample [14, 15]. Since this is not needed, the procedure in this thesis is limited to transferring the wires to a TEM sample grid and tilting the holder in order to observe the crystal structure.

1.3 Tomography on the nanoscale

Even though nanowires, as mentioned in section 1.2, are quite ideal samples for TEM there still can exist some ambiguity in how the images should be interpreted. A clear parallel can be made to tomography in medicine in which X-rays are used to image the inside of a human body instead of cutting it open. One observation will not resolve features along the projection (depth), perhaps leading the physician to the wrong conclusion. A natural way of preventing this is to gather additional data from different angles, which combined give more information. The concept of *computed tomography* (CT) in medicine is a way of calculating a 3D model from a setup specialized in acquiring images at specific angles around a body.

Since TEM, used in absorption mode, conceptually behaves the same way as X-rays, it is clear that tomography can be applied the same way for TEM, but with an improved resolution. Again, multiple images must be acquired but the microscope is too bulky for moving about and instead the sample is tilted. Patient comfort is not an issue in materials science the way it is in medicine.

Chapter 2

Growth of nanowires and characterization

In order to understand the importance of the analysis, some concepts on how the nanowires are grown must first be introduced. This chapter introduces the concept of epitaxy, how a supply of precursors can result in nanowires, and how a change in precursors affects the resulting nanowires. These basics are intended to help in understanding *Aerotaxy*, which is used to grow the wires analyzed here. Finally, some additional analysis techniques used, apart from TEM, are presented briefly.

2.1 The principle

Epitaxy

As discussed in section 1.1, nanowires offer novel ways of combining and adjusting materials not possible in bulk. A common method of crystal growth is through a process known as epitaxy. Here, this is achieved by a layer-by-layer growth in which a layer is grown on top of another layer keeping its crystal structure [7]. This is straightforward if the materials system remains the same, but can also work for heterostructures by straining of both the underlying and newly formed layer in order to make them *fit*. Epitaxy can be used to form high quality homo- or heterostructures in thin films, but also in nanowires [4, 5, 16].

In order for nanowires to form, a preference for nucleating growth at a confined area, over and over again without covering the rest of the surface must exist, at least not in

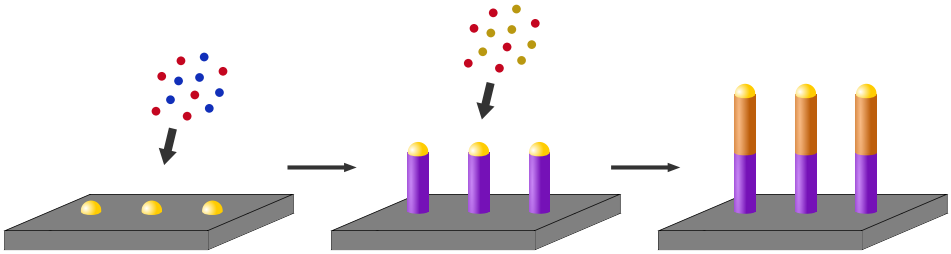

Figure 2.1: Growth of nanowires using a metallic droplet as the catalyst. Using two different combinations of precursors, an axial heterostructure is created (two different compositions along the wire).

the same rate, thus creating crystalline pillars or nanowires. The size of the area where nucleation is enhanced determines the width of the wire and the duration of growth determines the length. The confinement is either done as in figure 2.1 with a catalytic metallic droplet which confines the growth to its contact between the substrate and itself (catalyst-assisted growth), or by using some form of a mask [17].

Supply of precursors

In order to achieve growth, the constituents of the crystal must be continuously supplied, either in their pure form or as some form of precursor. Two of the more common ways of doing this is through *molecular beam epitaxy* (MBE) [4] or *metalorganic chemical vapor deposition* (MOCVD, sometimes called *metalorganic vapor phase epitaxy*, MOVPE) [4]. In MBE, the precursors are directionally supplied through a beam of a pure source of the elements in vacuum, while in MOCVD the precursors are gaseous compounds containing the components, for instance trimethylgallium (TMGa, $Ga(CH_3)_3$) for supply of Ga. In MOCVD the elevated temperature cracks the molecules, releasing the atom that is included in the growth. Fine-tuned growth parameters, such as temperature, total gas pressure and the respective molar fractions of the precursor gases will dictate the morphology and crystal structure of the resulting wire. If a metallic droplet is used as a catalyst, the component commonly takes the path of vapor to liquid (dissolving in the metallic droplet) to solid phase, giving rise to the name *vapor-liquid-solid* (VLS) growth. Here we generally refer to catalyst-assisted (Au) MOCVD VLS growth as it is low-cost and one of the more versatile techniques [7]. A common example is the formation of GaAs, with a general formula as:

$$(CH_3)_3Ga(g) \; + \; AsH_3(g) \; \xrightarrow{Au} \; GaAs(s) \; + \; 3\,CH_4(g)$$

2.2 Crystal structure

III–V semiconductor nanowires are generally observed to have two different crystals structures: *zincblende* (ZB) and *wurtzite* (WZ). Additional symmetries exist but are not very common for these growth conditions. III–V materials generally adopts the ZB crystal structure [11]. This is a cubic structure with the III-component adopting a *face centered cubic* (FCC) structure and the V-component at a position displaced $\frac{1}{4}, \frac{1}{4}, \frac{1}{4}$ relative to the III-component. This means that both components adopt FCC structures that are interwoven and the number ratio between them is 1:1. A second structure possible in III–V nanowires is WZ. However, this structure is not generally adopted in bulk III–V materials (except for III–N) but the geometries of the nanowires make it possible [11]. In this case the III-component adopts a *hexagonal close packed* (HCP) structure with the V-components shifted $0, 0, 0, \frac{3}{8}$ relative to the III-component (in the ideal case) [18].

Growth of III–V nanowires is generally done in a direction perpendicular to the close packed planes. This means that ZB is grown in a <111> and WZ in a <0001> direction [19, 20]. The difference between the two in terms of growth layers are the close packed layer order. Viewing one type of atom at the time, ZB is grown in a ABCABC progression while WZ is grown as ABABAB. Deviation from these are called stacking faults and can affect the properties, such as electrical conduction, of the structure [21, 22]. In figure 2.2 the two different structures are illustrated by ball-and-stick models and especially the differences are shown, highlighting layer order and projection along common observation directions, <110> and <11$\bar{2}$1> for ZB and WZ respectively.

2.3 Aerotaxy

Epitaxially grown III–V semiconductor nanowires have proved to be a useful way of producing fine-tuned nanowires with specific properties and with high crystallographic quality for high performance applications [23–25]. However, to apply nanowires and their advantages in industrial applications, not only should the final result be optimized, but the means of production must also be optimized for high yields and to be cost efficient. One promising method to achieve this is called Aerotaxy which basically is a way of growing nanowires from just the catalyst seed particle, without the need of a substrate. The particles are transported through a furnace with the precursor gases. Nucleation occurs from the particle and wires emerge, as illustrated in figure 2.3. The whole process is fast ($\sim$1 s) and continuous [26], which is an advantage for industry. Additionally, the single crystal substrates needed for epitaxial growth are expensive which means removing them reduces the cost further.

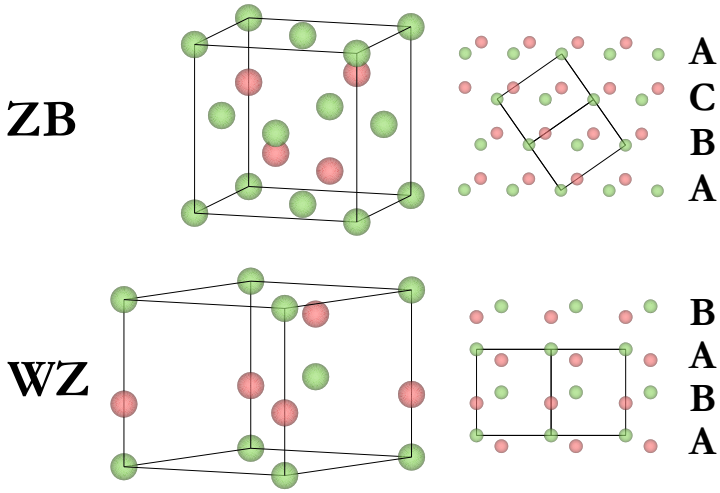

Figure 2.2: Crystal structures of zincblende (ZB) and wurtzite (WZ) shown in ball-and-stick models. The left-hand side shows the unit cells while the right-hand side shows them in their preferred observation direction in TEM, <110> and <11$\bar{2}$0> for ZB and WZ respectively.

The setup

The Aerotaxy setup consists of a number of sections that create and select the catalyst seed particles, perform the growth, and collect the wires. First an evaporation stage that heats Au at ∼1800 °C is used, followed by cooling in a flow of N_2 to form individual particles which are then sintered to form spheres. These spheres are then size selected in a *differential mobility analyzer* (DMA) to specify a certain particle diameter to be used in the growth stage.

The growth occurs by combining the precursor gases and the size selected particles and flowing these through a furnace. This however can be fine-tuned even further by having multiple stages at which different temperatures are used and additional precursors can be added in order to create heterostructures. The last section can be used to cool the wires in order to *finalize* the growth, instead of an abrupt quench. The formed wires can then be collected on a surface of choice when exiting the furnace setup. Such a surface can either be the intended use of the wires (such as panels for solar cell applications) or directly to substrates or TEM-grids for immediate analysis.

Development of Aerotaxy

The development of the Aerotaxy technique started with the production of III–V nanocrystals from aerosols of the III-component and addition of the V-precursor to

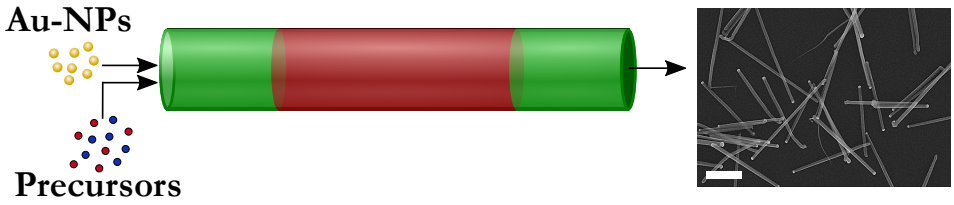

Figure 2.3: Schematic illustration of the Aerotaxy setup. The seed particles, in this case Au, are inserted in the furnace with the precursors. The furnace setup can be segmented to provide different temperature and addition of more precursors along the way. The image is a SEM image of collected nanowires. Scalebar is 1 µm. SEM-Image courtesy: Wondwosen Metaferia.

initiate growth during transport through a furnace. The method made it possible to produce size controlled nanoparticles of III–V material by controlling size selection of the aerosol particles, flow of the V-precursor, and growth temperature [27–30].

The next advancements made it possible to use a seed particle of a metallic catalyst and precursors of both the III- and the V-components, in this case Ga and As, to form nanowires with tunable properties of length, diameter and crystallographic quality, similar to what has been done using regular substrate based growth [26]. Following this, projects have achieved ternary III–V nanowires [31], *p*-doping using Zn [32], *n*-doping using Sn [paper III], and recently: *p-n* junctions [33].

2.4 Characterization techniques

Apart from the transmission electron microscope, other techniques have been used. This section briefly introduces the concepts of these additional techniques and what role they have in the analysis of nanowires. X-ray energy dispersive spectroscopy has been used in the TEM while photoluminescence and SEM were done in collaboration with researchers within NanoLund.

Photoluminescence

Photoluminescence, or PL, is a technique of exciting electrons using photons and measuring the emitted fluorescence to reveal the band structure of the sample. Semiconductors are characterized by a band gap, a gap in the possible energy states for the electrons where there can be no occupation. The band of states below and above the band gap are called the valence band and conduction band, respectively, and has full occupancy (valence band) or zero occupancy (conduction band) at its ground state (see figure 2.4a). PL makes use of the tightly spaced states above and below the band gap to measure the actual band gap by exciting electrons over the gap by exposure to

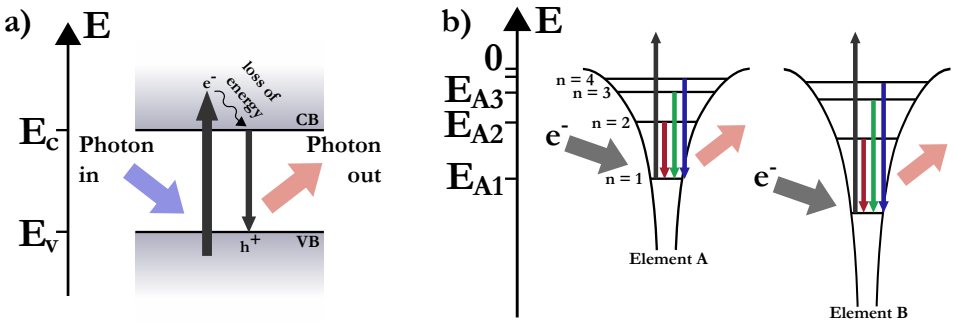

Figure 2.4: Illustration of the signal generation in PL (a) and XEDS (b). a) The incoming photon excites an electron from the valence band across the band gap. When the electron relaxes the emitted photon reveals the band gap width (E_c - E_v). Any shift of the bands will affect the emission energy. b) An incoming electron (in the case of EM) excites a core-electron. Higher energy electrons will relax and take its place. The emitted photon reveals the relative distances between the energy levels which is characteristic for each element.

high-energetic light, often a laser [34]. The incoming photon energy exceeds the band gap and the electron is lifted, creating its counter-particle, a hole, in the valence band. Through small emission-free energy loss, the electron loses energy to reach the lower edge of the conduction band. The hole behaves the exact opposite in the valence band and finally the two recombine over the band gap, emitting the photon energy related to the width of the gap [34]. Detection of this photon energy reveals the composition and band gap properties of the semiconductor (figure 2.4a).

The reason for it being useful in analyzing nanowires is the dependency on small changes in composition and band structure. For instance, if dopants are introduced, the electronic structure of the semiconductor will change, which can be detected using PL. *n*-doping, introduction of constituents containing extra electrons compared to the rest of the lattice, will create extra energy states within the band gap and will also cause an apparent shift (upwards) of the conduction band edge. The amount of doping will dictate the shift and can hence be quantified by PL.

X-ray energy dispersive spectroscopy

While PL exploits the band gap and its shift due to compositional changes, *X-ray energy dispersive spectroscopy* (XEDS) directly detects emissions from respective component (atoms) in the sample. As the name suggests XEDS detects and analyzes X-ray emission from the sample according to the energy of the emission. The emission is caused by excitations of core electrons in an atom by the interaction with incoming high-energy electrons, followed by a relaxation of a higher energy electron into the newly available state. The emitted X-ray energy relates to the spacing of core states of the atom, which is characteristic for each element [2, pp. 581-584]. The emitted en-

ergies correlate to $E_{A2} - E_{A1}$, $E_{A3} - E_{A1}$, etc for element A and the corresponding differences for element B shown in figure 2.4b.

In this thesis the XEDS technique has been used in combination with TEM, where the incoming beam is the excitation source. A specialized X-ray detector, fitted at an angle above the sample, detects the full spectra, and through analysis of peaks qualitative and quantitative data about the composition can be obtained.

The advantage of XEDS compared to PL is the flexibility. There's no need for a band gap structure and almost any atom can be detected, as long as it has a second energy state above the excited one (excludes H and He) and is not absorbed by any protective window of the detector (commonly made of Be, which also excludes Li and Be). However, low compositions are not possible to distinguish, much less quantify. The figure of uncertainty for quantification in XEDS is around 1 at% [2, p. 648], which means that doping levels can not be detected (lower than 0.01 at%) and PL is hence a good complement. Since XEDS analyzes core states' relative energy difference, information about their bonding chemistry will be lost due to these factors generally involves valence states.

Scanning electron microscopy

Scanning electron microscopy (SEM) is the most commonly used electron microscope technique. It is used to observe nanometer sized features and is capable of imaging the surface of *bulky* samples since it does not rely on any electrons being transmitted as in the case of TEM. The size limit of samples is set by the sample stage and what can be fitted into the vacuum chamber. Due to the varying sizes of samples possible to analyze it is a valuable technique for many different fields, including biology, nanomanufacturing and metallurgy [35, pp. 1-18].

The principle of SEM is not very different from *scanning TEM* (STEM), which will be explained in section 3.2, in which a fine probe of electrons is formed and rastered across the imaging area of the sample. In the case of SEM, however, the electrons have energies about one order of magnitude lower than in the TEM. The sample is most often thicker than what the electrons can reach, hence detectors above the sample are employed, which detect signals such as backscattered electrons (BSE), secondary electrons (SE) and characteristic X-rays (for XEDS analysis) [35, pp. 75-98,274-27].

SE are the most common imaging signal since these electrons have very low energy and can only escape from a small depth, to the advantage of resolution and surface sensitivity. Edges and creases of a surface provide more surface area for a SE to reach and hence will give strong surface topology contrast [35, p. 92]. BSE on the other

hand are the incoming electrons which have scattered in the sample and returned, escaping through the same surface as they entered. Since the BSE have only lost small amounts of energy they have much higher energy than the SE, which means they can escape from larger depths, reducing the spatial resolution. The amount of backscattered electrons greatly depends on the likelihood of them scattering against the sample atoms, and with higher atomic number the likelihood of scattering goes up, meaning higher atomic number showing up as more intense in the BSE signal [35, p. 75].

Chapter 3

Transmission electron microscopy

In this chapter, the concept of *transmission electron microscopy* (TEM) will be introduced and how the hardware is setup to be able to image samples, especially nanowires. The imaging is used both for regular micrographs and for the electron tomography presented in chapter 4.

The reason of using electron microscopy instead of visual light microscopy (VLM) is to overcome the limitation on resolution presented by the wavelength of light (δ_{VL}), called *Abbe diffraction limit*, which translates to about half the wavelength for visible light (λ_{VL}: $\sim$380-750 nm) [2, p. 5]. With a wavelength for electrons defined by de Broigle being much smaller (λ_e; 100 kV: 3.5 pm, 200 kV: 2.3 pm, 300 kV: 1.7 pm), this means an improved theoretical resolution.

3.1 The microscope

The purpose of a TEM is to obtain information of a sample by detection of electrons that have passed through it. Along the way, the electrons are affected by electromagnetic lenses which deflects their path in order to focus them into specific spots or to form images at certain distances from the sample. The system can roughly be divided into three parts; electron generation and lenses forming the beam (illumination lens system), the sample and the objective lens (imaging lens system), and the final lenses to magnify the image onto the detector (projection lens system). In figure 3.1 a photo and schematic drawing of one of the TEMs used in this thesis is shown. It is a Jeol 2200FS TEM and a special feature is the filter lens (FL) which can filter electrons by their energy (after losses). However, this feature has not been used in this thesis.

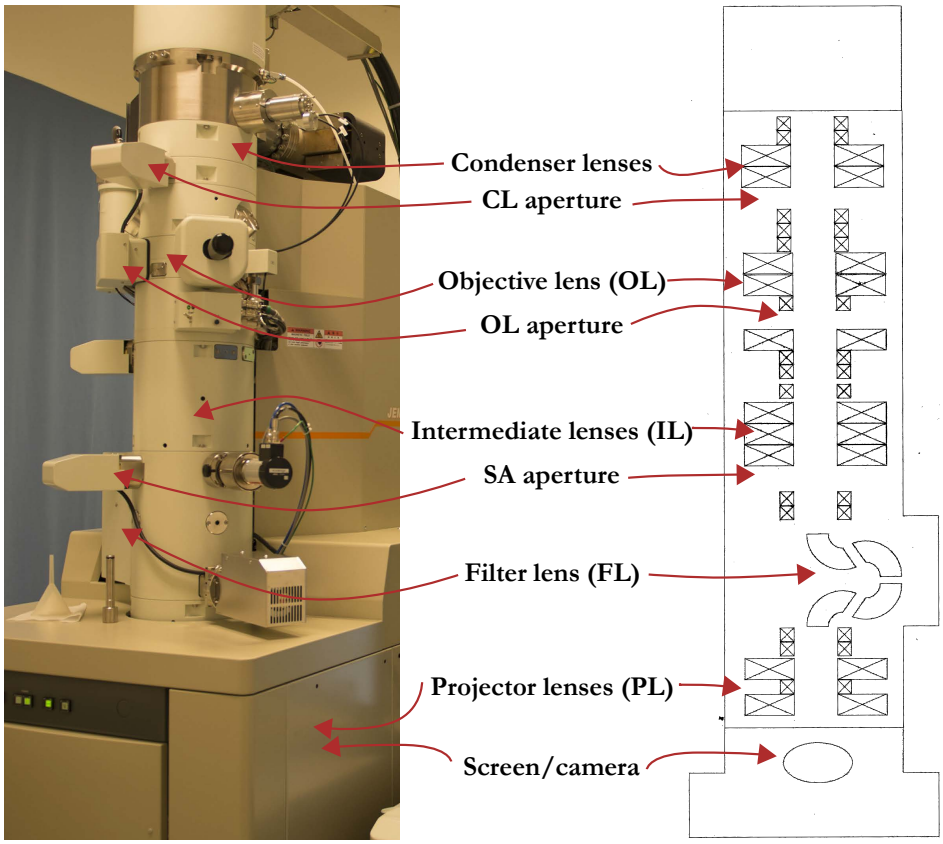

Figure 3.1: A photo and schematic drawing of a Jeol 2200FS TEM in Lund. The different lenses and locations of apertures are indicated by the arrows.

The *illumination lens system* includes the extraction of electrons from a source, the *gun*, acceleration of the electrons, and the initial lenses that form a beam of the extracted electrons before they interact with the sample. Conventionally, the guns have been heated metallic filaments which, at elevated temperatures (T), emit electrons. These filaments have to be able to withstand the temperatures at which the electrons could overcome the work function (ϕ_w) of the material, resulting in only a few candidates. W is one, LaB_6 another, where the former is cheaper and the latter has a lower work function, resulting in less heat needed and a reduced energy spread (δE) of the emitted electrons [2, p. 74]. However, in order to further reduce the energy spread for a more coherent source of electrons in microscopes that require this, *field emission guns* (FEG) are used. Such an electron gun consist of a very fine tip made of W, with a ZrO_2 layer. A powerful electric field is applied at the fine tip, *pulling* (tunneling) the electrons from the source. Such a procedure will greatly reduce the energy, as well a the spatial, spread of emitted electrons [2, pp. 74-76]. The FEGs come in two

Table 3.1: Comparison of electron guns: their respective operation temperature (T), work function (ϕ_w), and electron energy spread (δE) [2, p. 74].

	W	**LaB_6**	**Schottky-FEG**	**cold-FEG**
T /K	2700	1700	1700	300
ϕ_w /eV	4.5	2.4	3.0	4.5
δE /eV	3	1.5	0.7	0.3

flavors, heat assisted (Schottky-FEG) and non-heat assisted (cold-FEG). Schottky-FEGs reduces the need of gun cleaning by application of heat, sacrificing some energy spread, while a cold-FEG has lower energy spread but requires a gun flash (removal of contaminants on the tip by a short period of heating) after some time of use (a couple of minutes to a couple of hours, depending on the vacuum condition). A comparison of gun properties is presented in table 3.1. After extraction, the electrons are accelerated to the desired energy, commonly 200-300 keV, and through the use of the first lenses (condenser lenses) the electrons are collected according to the specified mode of operation (section 3.2) and can either project a parallel beam or a fine focused probe onto the sample.

The *imaging lens system* consists of the sample, which the electrons interact with, and arguably the most important lens overall in the TEM, the *objective lens* (OL). After interacting with the sample, the transmitted electrons with their possibly changed phase and scattering angle enter the objective lens which focuses these to a defined focal plane (a Fourier plane), followed by an image plane. This lens is responsible for the first collection of electrons after interaction with the sample, hence its importance [36].

After the sample and objective lens there are a series of lenses, intermediate and projection lenses, making up the *projection lens system*, which has the straightforward task of bringing one of the planes from the objective lens all the way to a detector. Here arises some differences depending on the mode of operation illustrated in figure 3.2. In the case of a parallel beam there will be two planes of interest for the TEM, a Fourier plane and an image plane. (a) In the first case, the projection lenses magnifies the Fourier plane to the detector, which reveals the diffraction pattern (DP) and spatial frequencies of the imaged area. (b) In the second case, an image plane is instead selected to be magnified and the result is an image. (c) Thirdly, if the microscope is operated in a scanning mode using a fine probe of electrons, the task of the projection lenses is to bring the transmitted electrons to a different kind of detector, which usually only measures the intensity as a function of scattering angle. The projection lenses are then used to define the angles.

Along the electron path there are also apertures which can select which electrons to include in the final image or diffraction pattern and block others. A *condenser aperture*

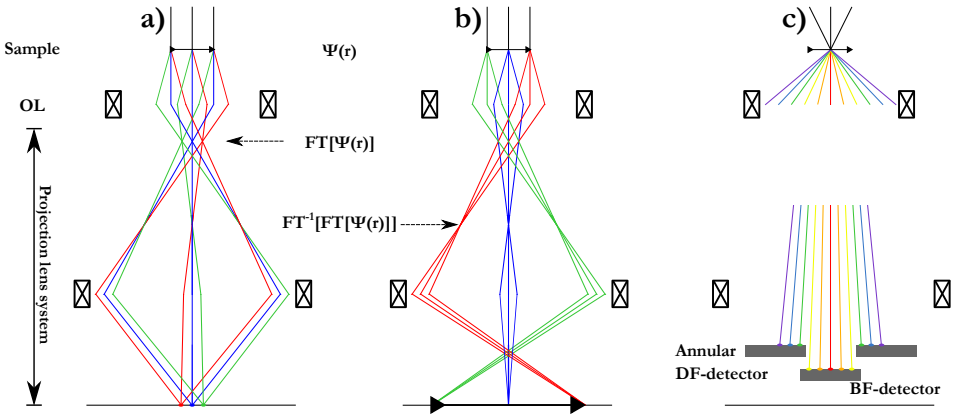

Figure 3.2: The three modes of operation in a regular TEM simplified to show as few lenses as possible. a) Formation of a diffraction pattern on the detector by magnification of a Fourier plane (arrow). b) Formation of an image on the detector by magnification of an image plane. c) A scanning probe is scattered when interaction with the sample. The different angles of scattering are transferred, either to a direct (bright field) detector or an annular (dark field) one. Note the only difference between a) and b) is which plane (arrow) is transferred to the detector. The focal plane is a Fourier transform (FT) of the image $\Psi_o(\mathbf{r})$ and the image plane is inversely Fourier transformed (FT^{-1}) of the focal plane.

(after the condenser lenses) can remove less coherent electrons at the cost of intensity, an *objective aperture* (after the objective lens) can be placed in the focal plane of the objective lens to select what specific spatial frequencies of the image to be included, and finally a *selective area aperture* (by the intermediate lenses) can select areas in the image (positioned in an image plane) to be included, mostly used for defining specific areas of which diffraction patterns that are to be evaluated.

3.2 Image formation and aberrations

In the TEM, the transfer of information is through detection of electrons that have passed through the sample, and the contrast between different areas is what makes up the image. Such electron detection can be performed in multiple ways but in the TEM it is common with semiconductor detectors and charge coupled devices [2, pp. 117-118]. The semiconductor detector (most often Si) is doped to form a *p-n junction*, the same principle as a solar cell. Such a detector will measure impinging electrons as a current to quantify the amount of electrons detected. For site specific detection however, *charge coupled devices* (CCD) are used. The electrons hit a detector surface where a fiber-optic array transfers the signals as photons (scintillator) onto the CCD where a digital image is recorded. The type of detector varies with microscope manufacturer and the purpose of the detector [2, pp. 120-121].

Conventional TEM

The TEM used in conventional (parallel) mode (CTEM) generally uses a CCD for detection of electrons in the plane that is projected onto it. For this mode, both absorption and phase contrast can be considered. For absorption contrast the electrons hit the sample and where there is thicker or denser parts there will be less transparency, due to both the absorption and more high-angle scattering outside the aperture, casting a darker shadow on the detector [2, p. 374]. However, phase contrast is capable of resolving much finer features, such as atomic lattices [2, p. 389] for *high resolution TEM* (HRTEM). The incoming electrons are treated as a wave hitting the sample. If the sample is thin enough, which is a reasonable approximation for many TEM samples, the wave exiting the object is only experiencing a slight shift in phase as a function of position, denoted as $\sigma V_t(\mathbf{r})$ (interaction factor σ and projected potential V_t), and the total wave is expressed as in equation 3.1 and the approximation is called the *weak phase object approximation* (WPOA) [2, 37, 38].

$$\Psi_o(\mathbf{r}) = exp\big[-i\sigma V_t(\mathbf{r})\big] \approx 1 - i\sigma V_t(\mathbf{r}) = 1 + \Psi_{so}(\mathbf{r}) \tag{3.1}$$

The process of focusing the transmitted electrons using the objective lens to its focal plane and back into an image in the image plane can be regarded as a Fourier transform (FT), into the focal plane followed by a inverse FT (FT^{-1}) back to the image (as shown in figure 3.2a and b). Here follows a mathematical approach on how this transfer occurs and especially how imperfections in the transfer will affect the final image. In order to reduce the amount of equations, they are described in appendix A on page 93, based on references [2, 37, 38] and summarized here.

We start with what is recorded in the image, intensity as a function of position, $I(\mathbf{r})$. This is related to the incoming image wave by its square. Through an approximation called *linear imaging approximation* the number of factors can be reduced to only include the ones that describe interaction between the direct beam and each scattered one, assuming interaction between scattered beams being much smaller, resulting in a linear problem. The approach is then to transform the equations into the frequency domain, $\mathbf{k}$. Since the image quality relies on how well features are resolved it is important that as high spatial frequencies as possible are transferred to the image. The intensity of each spatial frequency is described in equation 3.2 which depends on the Fourier transformed wave function of the scattered wave at the image, ψ_{si} (including its conjugate):

$$\mathcal{I}_i(\mathbf{k}) = \delta + \psi_{si}(\mathbf{k}) + \psi^*_{si}(\text{-}\mathbf{k}) \tag{3.2}$$

In an attempt to describe the transfer from object (ψ_o) to image (ψ_i) a couple of transfer functions are introduced. First an aperture function, A, that dictates a value of

which larger frequencies will be completely removed. Then a collective term, D, that dampens higher $\mathbf{k}$ due to imperfections in the setup which can be vibrations, energy spread of incoming electrons among others. Lastly, a phase shift term, $exp\big[-i\chi\big]$, is introduced. Through calculations and assumption regarding these functions one reaches the important conclusion:

$$\mathcal{I}_i(\mathbf{k}) \propto A(\mathbf{k})D(\mathbf{k})sin\big(\chi(\mathbf{k})\big) \tag{3.3}$$

The main result of all the derivations is that the resolution in the image is proportional to these components. Both A and D generally dampen higher $\mathbf{k}$, however, $sin\big(\chi\big)$ called the *phase contrast transfer function* (pCTF), affects lower $\mathbf{k}$ much more and is of interest for optimized day-to-day TEM work.

The factor χ is a sum of plural factors that change the quality of the transfer performed by the objective lens, and ideally: $sin\big(\chi\big) = -1$ to cancel the 1 from the direct beam. All lenses are affected to different degrees but since the objective lens performs the first magnification it is the most important. Equation 3.4 and 3.5 describes how χ depends on the different aberrations through the factors found in Appendix B on page 95 [39]. For non-hardware corrected TEM the major aberrations to consider are *defocus*, C_1, and *spherical aberration*, C_3 (equation 3.6) and the target of optimizing the pCTF is to keep the first crossover ($sin\big(\chi\big) = 0$, no transfer) as large as possible [39].

$$\chi(\mathbf{k}) = \frac{2\pi}{\lambda}W(\omega), \quad \omega = \lambda\mathbf{k} \tag{3.4}$$

$$W(\omega) = \Re\Big\{\sum\big[Aberration factor\big]\Big\} \tag{3.5}$$

$$\hat{\chi}(\mathbf{k}) = \pi C_1\lambda\mathbf{k}^2 + \frac{1}{2}\pi C_3\lambda^3\mathbf{k}^4 \tag{3.6}$$

In figure 3.3, the pCTF is shown for three different C_1 (0, -15, -30 nm) with a set C_3 (100 µm) from the Jeol 3000F TEM in Lund. By balancing equation 3.6 with an underfocus (negative C_1) the effect of the spherical aberration is reduced (-15 nm is the best of the three), until no longer possible. Figure 3.3 also shows the effect of the envelope function D (red curve in figure 3.3a) by combination according to equation 3.3 (resulting in the respective green curves beneath). The arrows mark the first crossover which is the resolution limit of the microscope with the specified aberrations. However, it is not the information limit since $sin\big(\chi\big) \neq 0$ for $\mathbf{k}$ larger than the resolution limit. These spatial frequencies will have a phase shift alternating from positive to negative, making images difficult to interpret. One way to circumvent this is by introducing the objective lens aperture (function A) which can be used to remove these frequencies that otherwise can contribute to the image in a way that is difficult to interpret as projected potentials.

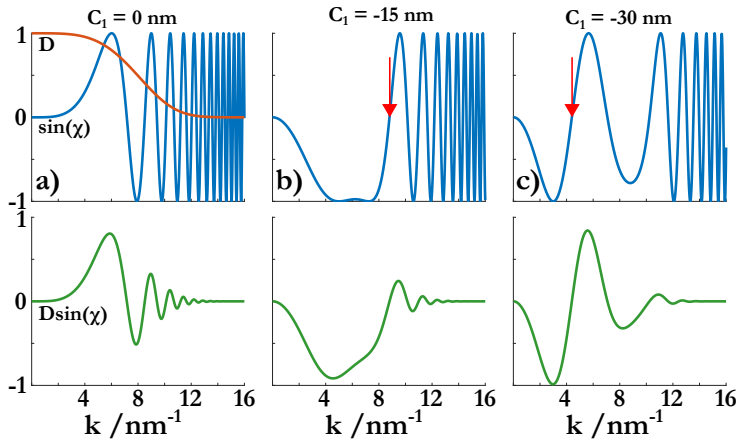

Figure 3.3: Illustration of the pCTF in the simple case of only considering defocus and spherical aberration. Three different defocuses (0, -15, and 30 nm) are shown. The green curves beneath are the result of combining $sin(\chi)$ and the dampening function D. It is seen that the best suited defocus in this case is -15 nm since the band of transmittance is optimal.

Scanning TEM

STEM, in contrast to CTEM, does not rely on the objective lens to the same extent. This is because the image is formed through focusing of the beam above the sample. Instead the illumination lens system determines the quality of the image since it is responsible for forming a fine probe onto the sample. When the probe is focused on the sample there will only be a small area that is illuminated at the same time. Since the probe is focused, the incoming electrons cannot be described as a plane wave but the main point is: The finer the probe, the better the resolution in the image and deviations from a perfect probe can be described in same terms of aberration as for CTEM but this time for the lenses prior to the sample. As shown in figure 3.2c, the projection lens system then brings the signal to two types of detectors, as a function on their scattering angle from the sample. One detector is situated in the direct beam (*bright field*, BF) while the other collects electrons scattered to a higher angle (*dark field*, DF). A comparison of the two types of images is shown in figure 3.4. The settings of the projection lens system dictates which angle will be the cutoff angle and the value is often given in *camera length* (CL) by tradition or more easily understood: collection angles (unit: mrad).

The image formation in STEM is done by scanning the probe across the sample and collecting intensities using the detectors (semiconductor detectors) from each site, which make up the pixels in the full image. Intensity at each pixel is determined by the intensity of signal at corresponding scattering angles that fall on the selected detector. When the electrons interacts with the sample, they can either pass straight

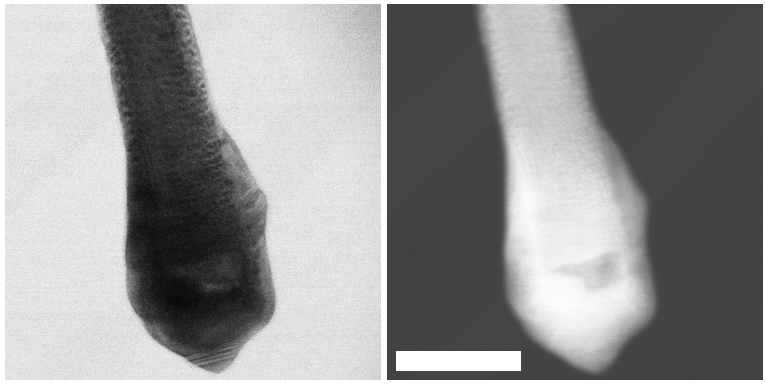

Figure 3.4: Comparison of a BF (left) and HAADF (right) image of a InAs nanowire with a GaSb shell. A small Au particle is also included (seen to the left of the dark central region in the DF image). In the DF image the thickness and composition is resolvable while the BF image also shows some diffraction contrast (stripes at the bottom and right side of the image). The scalebar is 100 nm. Image courtesy: Daniel Jacobsson.

through or interact elastically or inelastically with the sample. The direct and elastically scattered electrons diffract according to the sample structure while the inelastically scattered electrons scatter to even higher angles. The intensity to the BF detector will be reduced if the sample is thicker or denser but will also include contrast from the diffraction, such as differences in crystallography. The intensity on the *annular DF* (ADF) detector depends on the collection angles. In this case the intensity will increase with a thicker or denser sample, but also include some diffraction information. To avoid the diffraction contrast all together, and only detect inelastically scattered electrons, the collection angles must be higher than what the diffraction pattern is considered contributing to (it depends on the accelerating voltage and the specific sample). This is called *high angle ADF* (HAADF) and its intensity depends on the atomic number and thickness [2, pp. 379-380].

3.3 Aberration correction

Correcting for aberrations is vital for achieving higher spatial resolution [40]. Just as in equation 3.6 when C_1 is balanced to compensate for C_3, the same approach is used for more of the aberrations in appendix B on page 95. However the introduction of higher order negative aberrations to counteract others is slightly more advanced.

Hardware correctors are advanced sets of quadru-, hexa-, and octupole electromagnetic setups along the beam of the microscope. These setups can distort the beam and introduce the fine-tuned aberrations that are sought [40, 41]. For instance, a negative spherical aberration (C_3) can compensate a 5th order spherical aberration (C_5), and a negative twofold astigmatism (A_1) can compensate third-order-star aberrations (S_3)

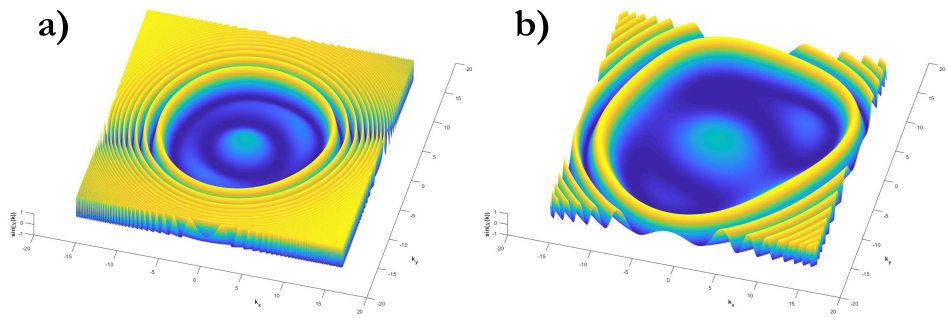

Figure 3.5: A surface plot showing the pCTF ($sin(\chi)$) as a function of two factors k_x and k_y in the plane. a) shows a scenario with C_3 = 100 µm while b) shows an aberration corrected microscope with C_3 = 19 nm. As can be seen some of the aberrations are not symmetrical around the center.

[40]. The one dimensional aberrations shown in figure 3.3 are just simple cases. Additionally there exists some radially asymmetrical aberrations, such as astigmatism or coma, which can be corrected for as well. Figure 3.5 shows such a case (real numbers from an aberration corrected Hitachi 3300 TEM in Lund), before (a) and after (b) correction.

3.4 Compositional analysis

One important capability of the TEM is the possibility to perform compositional analysis at high spatial resolution. By prior knowledge of the components, the contrast can be a good indication on qualitative composition which is very useful for quick overview and distinction of areas with possible different composition. Some TEMs have the possibility to filter electrons depending on energy loss. Such a loss can be related to present elements and be used for compositional analysis. The Jeol 2200FS in figure 3.1 have a special filter lens for such filtering, capable of producing spectra, *electron energy-loss spectroscopy* (EELS), or filtered imaging *energy filtered TEM* (EFTEM).

X-ray energy dispersive spectroscopy

In this thesis the compositional analysis is usually done through XEDS (see section 2.4). While working in STEM mode it is possible to collect a spectra at each individual pixel of an area, composing a compositional map, or possibly selecting and evaluating spectra for individual features. Trends can then be detected as well as quantitative measurements. The latter measurement uses models for the individual components and by comparing the real spectra, their respective contribution can be calculated.

Chapter 4

Electron tomography

Some of the image formation theory from the previous chapter is important in order to understand how the TEM can be used to generate images and other data used for tomographic reconstructions, but this chapter is mainly covering tomography as a concept. It touches upon the theory behind tomography and the algorithms used for reconstruction. In sections 4.3 and 4.4 however, the TEM and tomography are brought together to explain why electron tomography is such a useful technique for 3D analysis on the nanoscale.

4.1 The principle

Tomography as a technique is a way of combining projection data back into a virtual object, a *tomogram*. If enough projections are available, with varying observation angles, the tomogram will resemble the original object [42]. A dimensional approach would be to describe each projection as a projection from 3D into 2D, and that set of 2D data is reprojected, known as *backprojected*, to a 3D volume. The combination of all backprojections results in the 3D tomogram. To show 3D data on flat pages often requires very specific examples, so the easiest analogy would be to backproject 1D signals back into a 2D tomograms. This 2D tomogram can of course also be seen as a single slice of the 3D tomogram created from a single line in each projected image (2D).

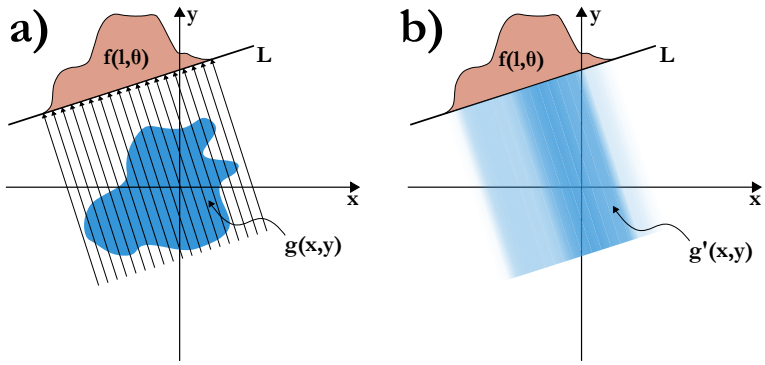

Figure 4.1: a) Illustration of the Radon transform from an object g to a projection f. b) The inverse Radon transform projects each projection (in the figure only one projection is shown) back to the object space (x, y) and the reconstruction $g'(x, y)$.

Radon transform

The underlying math about tomography was defined by Radon in 1917 [43, 44](the second reference is the translated version from German to English, published in 1986) which was later adapted for use in astronomy [45] and finally medical imaging using X-rays [46], which is closer to the application of tomography used in this thesis. Describing how to go from the object to the projection, Radon described a transform, known as the *Radon transform*. This transforms the object into a series of projections depending on the angle of projection, θ. For simplicity this is described in the 2D case with 1D projections in equation 4.1, which relates to figure 4.1. This transform represents the projections (figure 4.1a) but since the task of tomography is to do the opposite (figure 4.1b), the inverse transform (equation 4.2) is the one to use. δ is the Dirac delta function (being 1 only for $\delta(0)$ and 0 for the rest).

$$\mathcal{R}\big[g(x,y)\big] = f(l,\theta) = \iint g(x,y)\delta(xcos\theta + ysin\theta - l)dxdy \tag{4.1}$$

$$g'(x,y) = \iint f(l,\theta)\delta(xcos\theta + ysin\theta - l)dld\theta \tag{4.2}$$

Fourier space

Another way to consider tomography is to extend the concept of the Fourier transform to three dimensions (*Fourier space*). The Fourier transform of an object can perfectly describe the original object when inversely transformed, if the Fourier space is complete. When projection images of this object are acquired they reveal spatial frequencies in the specific plane and hence can describe a slice in the Fourier space (*Fourier slice theorem* [47]). The method of tomography, to acquire multiple projec-

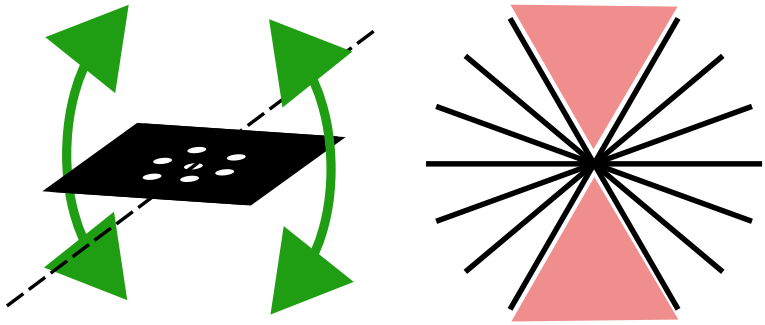

Figure 4.2: Illustration of building the Fourier space through tomography. Each projection makes up a slice in the Fourier space and when tilted the slice is tilted as well (green arrows). The missing wedge of information is shown as the pink triangles (wedge in 3D) and the spatial information from this parts will be missing.

tions of the object, can thereby build the Fourier space, slice by slice. Illustrated in figure 4.2.

The marked triangle in figure 4.2 shows the parts of the Fourier space that are missing due to not being able to project from + to - 90°. In three dimensions this triangle becomes a wedge and is known as the *missing wedge of information* [48, 49]. The missing spatial information leads to smearing of the reconstruction in that direction and is a important problem in tomography. Also the sparsity of the slices will affect the resulting Fourier space and hence the tomogram since the information in between the slices is lost. To improve the resulting tomogram, the missing wedge needs to be reduced and the Fourier space needs to be probed more finely [42]. In other words, a higher angle range covered, and a smaller increment between the acquisitions, will improve the tomogram. This has of course to be weighted against the time it takes to acquire many images, and possible restrictions in tilt range of the setup.

Projection requirement

One important aspect of the projections that are to be used in reconstructing the volume is the so called *projection requirement*, which states that the projected signal must be a monotonic function of a physical property [50, 51]. This means that the intensity of a signal must increase with the thickness along the projection and not change with the observation angle, which is a problem for diffraction contrast in crystalline samples [52]. Diffraction contrast will behave differently whether a crystal is observed on or off a zone-axis. Since the reconstruction assumes equal behavior of a point in the sample no matter the observation angle, and intensity is only differing when the projection includes more or less material in front or behind the point, diffraction contrast can trick the reconstruction and reduce its quality. All signals used in tomography must therefore fulfill the projection requirement.

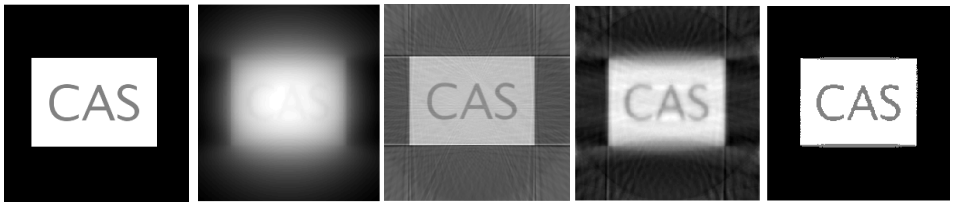

Figure 4.3: Comparison between four reconstruction algorithms. The original image is a box with text and has three different gray values furthest to the left. This is followed by the reconstructions from; BP, FBP, SIRT, and DART. The missing wedge of information is 18° for all of them.

4.2 Algorithms

The backprojection of the acquired images is a simple way of reconstruction but it has its clear limitations in smearing which has resulted in research on algorithms to circumvent these issues [53]. These algorithms have different advantages and disadvantages but a clear broader positive effect is the fact that the algorithms do not depend on the specific signal, but can be used in both X-ray or electron tomography [42, 54].

With the increased capabilities of computing power from modern computers, the interest in tomography and application of advanced algorithms has increased [55]. The calculations can be run with much higher speeds, making it possible to run multiple algorithms for comparison, or iterative algorithms that improve their output by each run [56, 57].

Backprojection

The simple *backprojection* (BP) builds on the inverse Radon transform and it performs an additive computation where the different projections are added back into the tomogram, one by one. This process inherently acts as a low-pass filter and general blurring will occur [49]. This is because the intensity in each projection is added to all pixels or voxels along its projection when backprojected, resulting in a smearing along that projection. A common way to improve the resolution is to counteract the low-pass filter by processing the projections with a high-pass filter of some sort before reconstructing using them [47]. Doing this, edges in the projection become more pronounced and the resulting tomogram will be less smeared. The filter itself can be of different kinds and optimized for the specific signal or sample. The actual value in each pixel or voxel does not have anything to do with any actual values at that point in the sample which is a drawback for quantitative analysis of the intensity.

Although some smearing still remains and the actual pixel/voxel values can be skewed,

the *filtered back projection* (FBP) is a very useful algorithm since it is simple and can act as a pre-reconstruction calculation to define which parts of the reconstruction are of interest. The distinction of what is of interest or not is especially relevant when the sample is a sheet, e.g. a cellular cut, and the volume above and below is empty.

Iterative reconstruction techniques

Another set of common algorithms are called *algebraic reconstruction techniques* (ARTs), which iteratively try to solve the difference between the initial projections and the projections from the tomogram [58]. The iterations uses backprojections and reprojections to improve the tomogram in order to result in a structure that, when projected, produces similar images as the original data. The result generally tends to reach an optimum after 20-40 iterations [55, 59].

One of the most common ones [59] of these is the *simultaneous iterative reconstruction technique* (SIRT) [56] which simultaneously projects the reconstructed object back to the original projections (Radon transform) in order to compare the projections. Comparing the new projections from the previous ones, a change $C_\theta^{q+1}(x, y)$ is computed for each pixel (x, y) in the 2D case (or x, y, z for 3D). Averaging this value, $\bar{C}$, for all projections (θ) one gets the change to be applied to every pixel. This is for one iteration (q) and for the next iteration $(q + 1)$ the new tomogram is the one to compare to [56].

$$\mathbf{g'}^{q+1}(x, y) = \mathbf{g'}^{q}(x, y) + \bar{C}^{q+1}(x, y) \tag{4.3}$$

One major advantage of SIRT is the improved reconstruction through the iterative process. However, smearing due to the missing wedge still exists. In contrast to BP and FBP, the SIRT reconstruction produces a value in each pixel or voxel which corresponds to an actual physical property [59]. For instance, if the signal depends on density according to a function, $\sum g(x, y)$ (summation along the projection), the reconstructed tomogram will also have values in each pixel or voxel depending on $g(x, y)$.

Other iterative techniques include *discrete algebraic reconstruction technique* (DART) which makes use of *a priori* (already known) information on how many intensity levels there are in the original object (discrete intensities). It uses a SIRT procedure but also assigns each pixel or voxel to the one of the discrete intensity levels. Using this technique has obvious disadvantages in the form lost gradients in the sample, but the major advantage is the reduced effect of the missing wedge [53, 55]. However, this requires information to start from, most easily retrieved from a pre-reconstruction using SIRT. The four presented techniques are presented in table 4.1 in terms of advantages,

Table 4.1: A comparison table of the four presented techniques and their advantages, disadvantages, and what the data actually shows.

Techniques	BP	FBP	SIRT	DART
Brief explanation	A simple technique of adding each projection as a projection back to the object.	Same as for BP but high-pass filtered in order to enhance sharp features such as edges.	Iterative technique that reprojects from the new reconstruction and compares with the original one in order to improve after each iteration.	Same as SIRT but with set discrete values that each voxel/pixel is assigned to.
Voxel/Pixel value	Sum of projections, no meaning	Sum of projections, no meaning	True value related to object	Value (discrete) related to object
Resolution	Poor	Improved	Good	Good
Missing wedge	Large effect	Large effect	Some effect	Less effect
Heavy calculations	No	No	Yes	Yes
Advantage	Easy and quick	Easy, quick and relative high contrast	Improving by each iteration	Same as SIRT, less effect from missing wedge
Disadvantage	Smeared tomogram	Still some smearing	Heavier calculations	Same as SIRT but also requires known discrete values

disadvantages and other properties, for easy comparison. Examples of reconstruction of a simple 2D image is shown in figure 4.3.

4.3 Tomography using a TEM

Now going back to what this thesis is about, analysis by electron microscopy, all the knowledge of tomography presented in this chapter can be applied to electron tomography. In this case the projections are micrographs from each projection angle and since the TEM can provide higher spatial resolution than, for example X-rays [49], this is promising for high resolution tomography.

The very controlled setup of a TEM is something that should not be rotated around a sample but instead the projections are acquired by tilting the sample. Regular TEMs usually have a small gap where the sample is inserted, which means the tilting is limited. Common tilting ranges are $\pm 60°$ or $\pm 30°$ or even less, depending on the type of microscope. However, using these numbers it is clear that a lot of the tomographic

information gets lost. Only 2/3 or 1/3 respectively of the Fourier space is actually possible to retrieve using these tilt ranges, which raises the need of special microscopes. In Lund there is a Jeol 2200FS TEM which, in combination with a smaller kind of sample holder tip, can tilt to around $\pm 81°$, which obviously is a much better solution, and it makes electron tomography meaningful. There also exist TEMs in combination with sample preparation that can tilt a full $\pm 90°$, which completely removes the missing wedge of information [60]. However, this requires the sample to be completely free from shadowing form both sample holder and sample support. This can be achieved by forming a fine tip of the sample and mounting it so it protrudes at the tip of the sample holder along the tilt-axis.

The projection requirement in the TEM

The previously mentioned requirement for the signal in a tomographic reconstruction (projection requirement), stating that the signal should be monotonic with a physical property [61–63], must be considered in the TEM. Absorption contrast reflects the amount of electron scattering in the sample; the higher density the material has, the lower the signal gets. Such a signal depends both on the density of the sample and the thickness, which fulfills the projection requirement. However if diffraction contrast is part of the image there will be a violation of this requirement since the intensity that each point in the sample contributes to the projection will vary, depending on the observation angle.

Amorphous samples that do not show any diffraction contrast can be imaged using conventional TEM while for crystalline samples imaging using CTEM is not possible. This means other imaging signals must be used, and luckily TEMs have multiple imaging signals that fulfill the projection requirement and can be used instead [63, 64]. A common choice is HAADF-STEM [64], which, since it only uses inelastically scattered electrons, does not contain any diffraction contrast but rather an intensity depending on density at each point in the sample. With the introduction of probe aberration correction this has even led to atomic resolution in tomographic reconstructions [65] which is of course is a major development and approaches one of Richard Feynman's old challenges [42].

Since the TEM is such a multi-signal instrument, the possibilities are endless in employing other signals and combining these for tomographic reconstructions as well. XEDS is such a signal, since the emission depends on the concentration at a specific point in the sample [64]. This is not entirely true due to absorption depending on depth from surface, but there are models to work around this as well [66]. Also different forms of *electron energy loss spectroscopy* (EELS) and *energy filtered TEM* (EFTEM) signals can provide data possible to use in tomography [67]. In the end, the possi-

bilities are endless for the TEM and with improved models of signal generation and detection, such as the case for XEDS, more signals and combinations of signals can be used. This makes electron tomography an even more promising technique for many different areas.

4.4 Post-processing

The resulting data from a tomographic reconstruction is a 3D (from 2D projections) or a 2D matrix (from 1D projections). The volume or image contains voxels or pixels with varying intensity depending on the intensity from the backprojected data. The property you choose as input will dictate the intensity in the reconstruction. For instance if you use density or compositional concentration as input, the output data will be the corresponding property. It is thus important to know the origin of the data and the method of reconstruction to be able to analyze the tomogram.

As in all imaging sciences, qualitative data from ET is quite easy to obtain. The human brain is an excellent tool for evaluation, but comparative data usually requires numbers, which are not as straightforward as just observing an image. The *segmentation* method is an important tool for assigning a category to each voxel or pixel. Using segmentation it is possible to count numbers of voxels or pixels of a certain kind, making numerical data available for comparison between samples or segments within the same sample.

Segmentation can be performed by simple intensity assignment. If a voxel's or pixel's intensity is within a certain range then it is assigned to a certain class. Alternatively, *graph-cut* can be applied if consideration is to be taken of neighboring pixels or voxels. This technique introduces penalties for assigning two different categories next to each other, which results in smoother transitions between segments, and fewer singular pixels or voxels with a different assignment from all its neighbors [68]. If the sample on the other hand contains multiple occurrences (e.g. particles) with the same intensity, these can also be segmented from each other in order to treat these as separate objects. A common method to do this is the *watershed segmentation*. In the 2D case this segmentation treats an image as a topology depending on the intensity. The segmentation divides the image along ridges (for dark objects on light background) or valleys (for light objects on dark background) [69] in order to assign certain pixels or voxels to belong to a certain class. The same principle is used for 3D objects, adding another dimension.

Chapter 5

Results and outlook

Using the TEM techniques described in chapters 3 and 4 to analyze nanowires, especially those grown by Aerotaxy (section 2.3), I have produced scientific data, some published and some in manuscript form which are included as papers I to III. In this chapter the previous chapters will be connected to each specific analysis which are included in the papers. The data is presented sorted by the different type of analysis; crystal structure, compositional analysis, and tomographic reconstructions. Finally some outlook on what is to come for my TEM research will be presented.

5.1 Crystal structure

Structural analysis in this thesis have consisted of distinguishing the structure of nanowires and evaluating their crystal quality by evaluating the number of stacking faults or other kinds of defects. Nanowires are quite ideal samples due to their thickness, making it possible to image them directly by HRTEM. The HRTEM micrographs have been used as in paper I to correlate which direction is which. This is of interest when correlating tomograms to the actual crystallographic directions, as in paper I. When the HRTEM micrograph identifies the observation direction as (110) at a specific sample tilt, that can be used in the tomogram as a setpoint. The edges (facets) can then be determined to be of e.g. {111}. There exist two such facets, A and B, determined by the terminating component (III or V respectively). Aerotaxy nanowires are known to grow in a <111>B direction [26] and hence the specific planes can be identified as A or B. It was found that the droplets that covered the surface of these wires were only found on the {111}B facets. Figure 5.1 shows an HRTEM micrograph with the beam parallel to the edge of a nanowire where the droplets are visible.

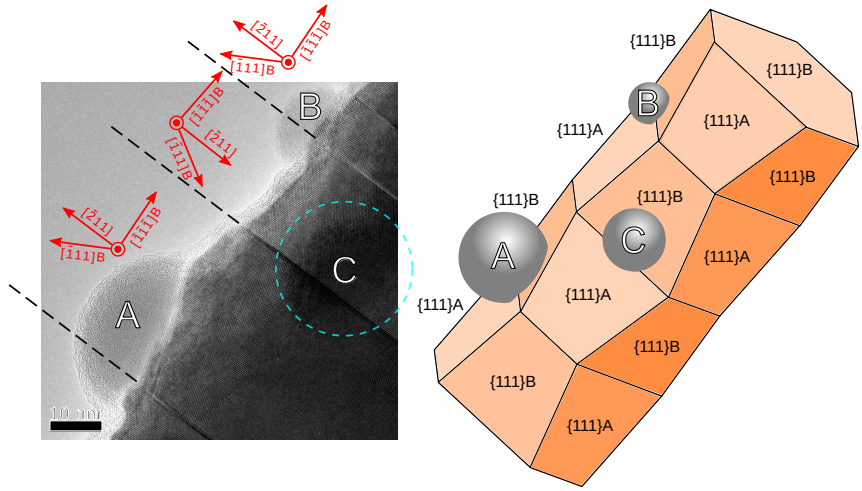

Figure 5.1: A high resolution TEM image to the left showing some surface droplets. The red arrows and labels show the crystal directions between the twin planes, illustrating that the droplets are only located on the {111}B surfaces. To the right there is a 3D drawing of the area. Droplet C can be seen as a faint shadow in the TEM micrograph. From paper I.

The growth direction was toward the top right and an illustration is shown next to the HRTEM micrograph, showing that the droplets appear only on the {111}B surfaces.

Using HRTEM, stacking faults can be clearly observed (figure 5.2) as done in paper II. The red arrows mark these features, which can be seen as sharp lines in the micrographs. A *fast Fourier transform* (FFT) (figure 5.2c) of the crystal structure reveals a twinning at each of the stacking faults, seen by the FFT being mirrored. Also, the stacking fault density can be qualitatively assessed to be increasing with changing growth conditions as in done in paper III (figure 5.3). In paper III the crystallographic analysis also revealed radial growth seen in figure 5.2d as a layer of ZB with high density of stacking faults. Also some branches, having the ZB structure were found. All the Aerotaxy wires analyzed in all the papers have had the ZB crystal structure, i.e. no WZ was found. A question for the future is if Aerotaxy has the capability to produce WZ nanowires the same way as in substrate based growth.

5.2 Compositional analysis

To evaluate the compositions of different nanowires, the TEM was used in STEM mode in combination with an XEDS detector. This makes it possible to produce element maps, acquire linescans of compositional trends, and perform quantitative analysis in specified points. The analysis of the wires in paper I showed most surprisingly that the droplets on the surface were Ga as seen in the maps in figure 5.4.

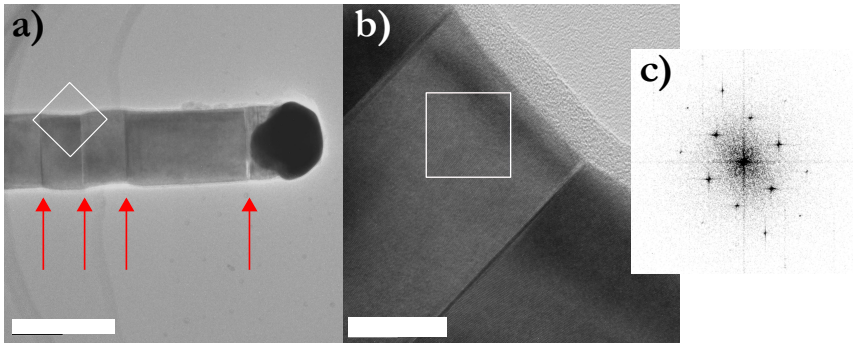

Figure 5.2: HRTEM micrographs of a nanowire grown by Aerotaxy. The white squares indicate where the next image or FFT is acquired from. Scalebars are 100 and 20 nm respectively. Adapted from paper II.

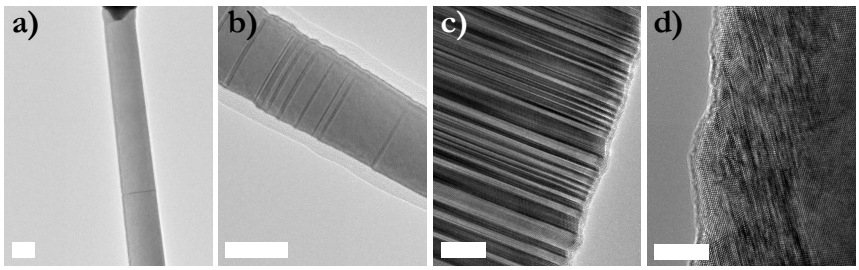

Figure 5.3: HRTEM micrographs of four nanowires grown in Aerotaxy but with different growth conditions. The result is a difference in stacking fault density. Scalebars are 50, 50, 10, and 10 nm respectively. Adapted from paper III.

For paper II and III the analysis consisted of analyzing the grown wires and their composition as a function of growth parameters, temperature and molar fractions (paper II), and quantitative analysis of the seed particles as a function of dopant precursor concentration (paper III). One example of a trend from paper II is shown in figure 5.5a where some noise is visible but generally the composition (of Ga, As, and P) stays stable throughout the growth. In paper III the composition of interest was the dopant Sn in GaAs (*n*-doping) which incorporates in too low concentrations to be evaluated by XEDS. Instead the compositions in the seed particles were evaluated to find a correlation with precursor concentration, concentration in the seed particle, and the doping levels (measured by PL).

Additionally to the XEDS analysis, the HAADF micrographs also provided substantial compositional data due to the signal being a function of atomic number. The heavier the atoms the more they scatter (higher intensity in HAADF) and this will reveal different phases in the sample. However, as seen in figure 5.5b from paper II apparently some diffraction contrast took part in the HAADF signal since the composition did not differ between the darker and brighter parts of the wire.

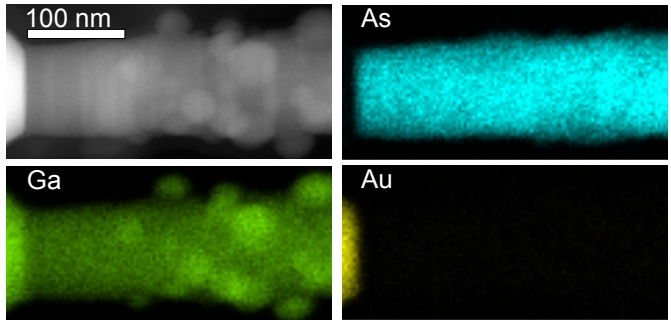

Figure 5.4: XEDS maps of the top part of a nanowire grown by Aerotaxy. The compositional analysis reveals that the nanowire contains Ga and As. The droplets on the surface contains Ga and the seed particle (left) is composed of Ga and Au. From paper I.

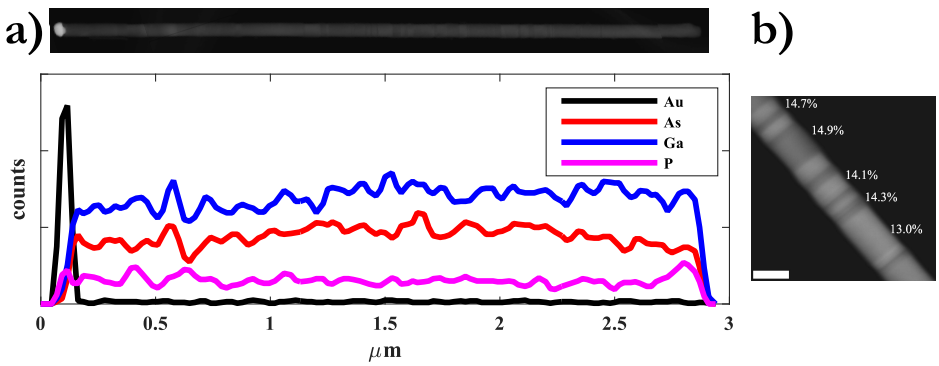

Figure 5.5: a) Compositional trend along a GaAsP nanowire. The levels are stable through the whole wire. b) A quantification of P illustrating the contrast in the HAADF-signal not belonging to compositional changes. From paper II

5.3 Tomographic reconstructions

ET analysis was performed in paper I for the Aerotaxy wires forming Ga droplets on their surface. This was done by acquiring micrographs from multiple tilts and then performing a reconstruction using the SIRT algorithm in the ASTRA Toolbox for MatLab [62, 70, 71]. The 3D analysis proved useful in showing where the droplets were positioned, something that was otherwise lost or ambiguous in regular projections. The question whether the droplets were on the front or backside of the wire could now be resolved and the whole cross-sectional profile could be evaluated (figure 5.6). However, since the tomographic reconstructions are from STEM-HAADF micrographs, the intensity in the tomogram depend on the atomic number (Z) and

the difference between Ga (the surface droplets) and GaAs (wire) is too small to be distinguished in the tomogram. This illustrates the need of sometimes applying compositional tomography (such as XEDS) instead of or in combination with STEM-HAADF.

Aware of the difficulty of illustrating 3D data in 2D, I developed a way of illustrating the surface, which to my knowledge has not been used before. The method consists of producing a tomogram, segmenting what is a wire (including the Ga droplets) and what is not (background), using either watershed or graph-cut segmentation, and finally for each cross section along the wire measure the radial thickness at each azimuthal angle. The result is a azimuthal map showing the topology of the wire as a function of distance along the wire and the azimuthal angle. This is a very useful tool for evaluating symmetrically occurring surface features, like the Ga droplets in paper III (figure 5.6).

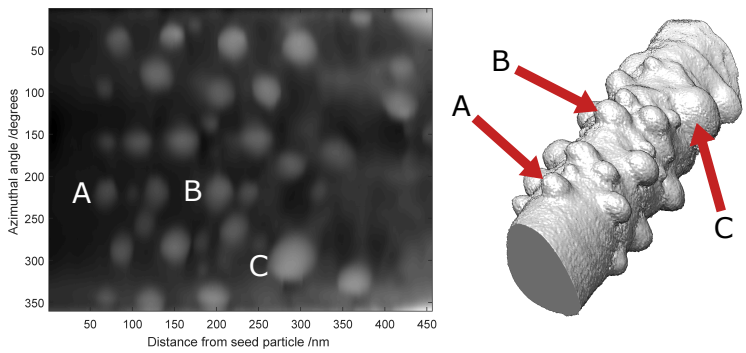

Figure 5.6: A tomographic reconstruction of an Aerotaxy nanowire with droplets on its surface. The surface topology is illustrated by an azimuthal map (left) which shows the connection between the crystallographic orientation, and the positioning of the surface features. Three droplets A-C are marked in both views to help the reader. Adapted from paper I.

5.4 Outlook

What I want to focus on in the future are two things: electron tomography, to create 3D images containing new information, not primarily about topology, and, in-situ microscopy, which answers the questions about how chemical reactions proceed on the atomic scale. I think that tomographic data makes objects easier to understand and interpret, especially nanostructure designs, and with improved reconstruction algorithms and higher resolution in the microscopes, this is a promising field. In the TEM, tomography has the advantage of being able to use multiple signals that are possible to reconstruct. However, in-situ microscopy can tell a lot more of the story behind how the atoms arrange in a specific way. Some form of time-resolved electron

tomography would be a dream come true. Imagine being able to follow the nucleation events of, for instance, nanowire growth in 3D. Perhaps using a quick acquisition as in [72], but doing it continuously to capture a process.

An ideal type of project for my final years of PhD studies would involve in-situ microscopy, especially nucleation events. For instance it would be interesting to look into the initial growth phase, and nucleation of the first part of an III–V crystal from an Au catalyst particle using in-situ microscopy. These early-stage nanowires, mimicking Aerotaxy growth (due to not nucleating from a crystalline surface) would be very interesting to analyze using electron tomography. Even if the tomography itself is not time-resolved, many tomograms of varying degree of nanowire initiation could give a fuller story.

References

[1] D. R. Askeland and P. P. Fulay. *Introduction to Materials Science and Engineering*. Second. Stamford: Cengage Learning, 2010.

[2] D. B. Williams and C. B. Carter. *Transmission Electron Microscopy: A Textbook for Materials Science*. 2009.

[3] Y. Chen, X. An, and X. Liao. "Mechanical behaviors of nanowires." *Appl. Phys. Rev.* 4.3 (2017).

[4] Y. Zhang, J. Wu, M. Aagesen, C. Zhang, X. Miao, K. D. Chabak, and X. Li. "A review of III–V planar nanowire arrays: selective lateral VLS epitaxy and 3D transistors." *J. Phys. D Appl. Phys* 50.39 (2017).

[5] Z. Mi and Y.-L. Chang. "III-V compound semiconductor nanostructures on silicon: epitaxial growth, properties, and applications in light emitting diodes and lasers." *J. Nanophotonics* 3.1 (Jan. 2009).

[6] Y. Xing, P. Han, S. Wang, P. Liang, S. Lou, Y. Zhang, S. Hu, H. Zhu, C. Zhao, and Y. Mi. "A review of concentrator silicon solar cells." *Renew. Sustain. Energy Rev.* 51 (Nov. 2015), pp. 1697–1708.

[7] K. A. Dick. "A review of nanowire growth promoted by alloys and non-alloying elements with emphasis on Au-assisted III–V nanowires." *Prog. Cryst. Growth Charact. Mater.* 54.3-4 (Sept. 2008), pp. 138–173.

[8] E. A. Fitzgerald and N. Chand. "Epitaxial Necking in GaAs Grown on Prepatterned Si Substrates." *J. Electron. Mater.* 20.10 (1991), pp. 839–853.

[9] K. L. Kavanagh. "Misfit dislocations in nanowire heterostructures." *Semicond. Sci. Technol* 25 (2010), pp. 24006–7.

[10] M. W. Larsson, J. B. Wagner, M. Wallin, P. Håkansson, L. E. Fröberg, L. Samuelson, and L. R. Wallenberg. "Strain mapping in free-standing heterostructured wurtzite InAs/InP nanowires." *Nanotechnology* 18 (2007).

[11] F. Glas, J.-C. Harmand, and G. Patriarche. “Why Does Wurtzite Form in Nanowires of III-V Zinc Blende Semiconductors?” *Phys. Rev. Lett.* 99.14 (2007).

[12] D. Danino. “Cryo-TEM of soft molecular assemblies.” *Curr. Opin. Colloid Interface Sci.* 17.6 (Dec. 2012), pp. 316–329.

[13] P. L. Stewart. “Cryo-electron microscopy and cryo-electron tomography of nanoparticles.” *Wiley Interdiscip. Rev. Nanomedicine Nanobiotechnology* 9.2 (2016).

[14] M. H. F. Overwijk, F. C. van den Heuvel, and C. W. T. Bulle-Lieuwma. “Novel scheme for the preparation of transmission electron microscopy specimens with a focused ion beam.” *J. Vac. Sci. Technol. B Microelectron. Nanom. Struct.* 11.6 (Nov. 1993), pp. 2021–2024.

[15] M. Winey, J. B. Meehl, E. T. O’Toole, and T. H. Giddings. “Conventional transmission electron microscopy.” *Mol. Biol. Cell* 25.3 (Feb. 2014), pp. 319–323.

[16] S. Lehmann, J. Wallentin, D. Jacobsson, K. Deppert, and K. A. Dick. “A general approach for sharp crystal phase switching in InAs, GaAs, InP, and GaP nanowires using only group V flow.” *Nano Lett.* 13.9 (2013), pp. 4099–4105.

[17] R. R. LaPierre, A. C. E. Chia, S. J. Gibson, C. M. Haapamaki, J. Boulanger, R. Yee, P. Kuyanov, J. Zhang, N. Tajik, N. Jewell, and K. M. A. Rahman. “III-V nanowire photovoltaics: Review of design for high efficiency.” *Phys. status solidi - Rapid Res. Lett.* 7.10 (Oct. 2013), pp. 815–830.

[18] C.-Y. Yeh, Z. W. Lu, S. Froyen, and A. Zunger. “Zinc-blende - wurtzite polytypism in semiconductors.” *Phys. Rev. B* 46.16 (1992).

[19] J. Johansson, L. S. Karlsson, C. Patrik, T. Svensson, T. Artensson, B. A. Wacaser, K. Deppert, L. Samuelson, and W. Seifert. “Structural properties of 111B-oriented III–V nanowires.” *Nat. Mater.* 5 (2006), p. 574.

[20] H. J. Joyce, J. Wong-Leung, Q. Gao, H. Hoe Tan, and C. Jagadish. “Phase Perfection in Zinc Blende and Wurtzite III-V Nanowires Using Basic Growth Parameters.” *Nano Lett.* 10 (2010), pp. 908–915.

[21] J. E. Northrup and M. L. Cohen. “Electronic structure of the rotation twin stacking fault in P-ZnS.” *Phys. Rev. B* 23.6 (1981), p. 2563.

[22] M. S. Miao, S. Limpijumnong, and W. R. L. Lambrecht. “Stacking fault band structure in 4H–SiC and its impact on electronic devices.” *Appl. Phys. Lett* 79.4360 (2001), p. 4360.

[23] B. Hua, J. Motohisa, Y. Kobayashi, S. Hara, and T. Fukui. “Single GaAs/GaAsP coaxial core-shell nanowire lasers.” *Nano Lett.* 9.1 (2009), pp. 112–116.

[24] Y. Zhang, M. Aagesen, J. V. Holm, H. I. Jørgensen, J. Wu, and H. Liu. "Self-catalyzed GaAsP nanowires grown on silicon substrates by solid-source molecular beam epitaxy." *Nano Lett.* 13.8 (2013), pp. 3897–3902.

[25] D. Jacobsson, S. Lehmann, and K. Dick. "Zincblende-to-wurtzite interface improvement by group III loading in Au-seeded GaAs nanowires." *Phys. Status Solidi - Rapid Res. Lett.* 7.10 (Oct. 2013).

[26] M. Heurlin, M. H. Magnusson, D. Lindgren, M. Ek, L. R. Wallenberg, K. Deppert, and L. Samuelson. "Continuous gas-phase synthesis of nanowires with tunable properties." *Nature* 492.7427 (2012), pp. 90–94.

[27] K. Deppert, J.-O. Bovin, J.-O. Malm, and L. Samuelson. "A new method to fabricate size-selected compound semiconductor nanocrystals: aerotaxy." *J. Cryst. Growth* 169.1 (1996), pp. 13–19.

[28] K. Deppert and L. Samuelson. "Self-limiting transformation of monodisperse Ga droplets into GaAs nanocrystals." *Appl. Phys. Lett.* 1409 (1996), pp. 10–13.

[29] M. H. Magnusson, K. Deppert, J.-O. Maim, C. Svensson, and L. Samuelson. "Size-selected GaN and InN nanocrystals." *J. Aerosol Sci* 28 (1997), pp. 47–472.

[30] K. Deppert, R. H. Martin Magnusson, L. Samuelson, J.-O. Malm, S. Chatrin SvenssonS, and J.-O. Bovin. "Size-selected nanocrystals of III-V semiconductor materials by the Aerotaxy method." *J. Aerosol Sci* 296.5 (1998), pp. 737–748.

[31] W. Metaferia, A. R. Persson, K. Mergenthaler, F. Yang, W. Zhang, A. Yartsev, R. Wallenberg, M.-E. Pistol, K. Deppert, L. Samuelson, and M. H. Magnusson. "GaAsP Nanowires Grown by Aerotaxy." *Nano Lett.* 16.9 (2016), pp. 5701–5707.

[32] F. Yang, M. E. Messing, K. Mergenthaler, M. Ghasemi, J. Johansson, L. R. Wallenberg, M.-E. Pistol, K. Deppert, L. Samuelson, and M. H. Magnusson. "Zn-doping of GaAs nanowires grown by Aerotaxy." *J. Cryst. Growth* 414 (2015), pp. 181–186.

[33] E. Barrigo, O. Hultin, D. Lindgren, F. Yadegari, M. H. Magnusson, L. Samuelson, L. I. M. Johansson, and M. T. Björk. "GaAs Nanowire pn-Junctions Produced by Low-Cost and High- Throughput Aerotaxy." *Nano Lett.* (2017).

[34] J. V. Behren, M. Wolkin-Vakrat, J. Jor, and P. M. Fauchet. "Correlation of Photoluminescence and Bandgap Energies with Nanocrystal Sizes in Porous Silicon." *J. Porous Mater.* 7 (2000), pp. 81–84.

[35] J. Goldstein, D. E. Newbury, D. C. Joy, C. E. Lyman, P. Echlin, E. Lifshin, L. Sawyer, and J. R. Michael. *Scanning Electron Microscopy and X-ray Microanalysis*. Third. New York, NY: Springer, 2003, p. 689.

[36] J. M. Rodenburg. “Understanding Transmission Electron Microscope Alignment: A Tutorial.” *Microsc. Anal.* (2004), pp. 9–12.

[37] A. I. Kirkland and R. R. Meyer. ““Indirect” High-Resolution Transmission Electron Microscopy: Aberration Measurement and Wavefunction Reconstruction.” *Microsc. Microanal.* 10 (2004), pp. 401–413.

[38] R. Meyer, A. Kirkland, and W. Saxton. “A new method for the determination of the wave aberration function for high resolution TEM: 1. Measurement of the symmetric aberrations.” *Ultramicroscopy* 92.2 (July 2002), pp. 89–109.

[39] R. Erni. “Aberrations.” *Aberration-Corrected Imaging Transm. Electron Microsc.* 2010. Chap. Aberration, pp. 189–228.

[40] M. Haider, P. Hartel, H. Müller, S. Uhlemann, and J. Zach. “Current and future aberration correctors for the improvement of resolution in electron microscopy.” *Philos. Trans. A. Math. Phys. Eng. Sci.* 367.1903 (2009), pp. 3665–82.

[41] A. Bleloch and A. Lupini. “Imaging at the picoscale.” *Mater. Today* 7.12 (2004), pp. 42–48.

[42] Z. Saghi and P. A. Midgley. “Electron Tomography in the (S)TEM: From Nanoscale Morphological Analysis to 3D Atomic Imaging.” *Annu. Rev. Mater. Res.* 42 (2012), pp. 59–79.

[43] J. Radon. “Über die Bestimmung von Funktionen durch ihre Integralwerte längs gewisser Mannigfaltigkeiten.” *Berichte über die Verhandlungen der Königlich-Sächsischen Akad. der Wissenschaften zu Leipzig, Math. Klasse* 69 (1917), pp. 262–277.

[44] J. Radon. “On the determination of functions from their integral values along certain manifolds.” *IEEE Trans. Med. Imaging* 5.4 (1986), pp. 170–176.

[45] R. N. Bracewell. “Strip Integration In Radio Astronomy.” *Aust. J. Phys.* 9 (1956), p. 198.

[46] A. M. Cormack. “Representation of a Function by Its Line Integrals, with Some Radiological Applications.” *J. Appl. Phys.* 34.9 (1963), p. 2722.

[47] M. Radermacher. “Weighted Back-projection Methods.” *Electron Tomogr.* 2nd. New York, NY: Springer, 2007. Chap. Weighted B, pp. 83–111. arXiv: `arXiv:1011.1669v3`.

[48] J. Zečevi, K. P. De Jong, and P. E. De Jongh. “Progress in electron tomography to assess the 3D nanostructure of catalysts.” *Curr. Opin. Solid State Mater. Sci.* 17 (2013), pp. 115–125.

[49] J.-J. Fernandez. “Computational methods for electron tomography.” *Micron* 43.10 (2012), pp. 1010–1030.

[50] I. Arslan, J. R. Tong, and P. A. Midgley. "Reducing the missing wedge: High-resolution dual axis tomography of inorganic materials." *Ultramicroscopy* 106 (2006), pp. 994–1000.

[51] A. J. Koster, R. Grimm, D. Typke, R. Hegerl, A. Stoschek, J. Walz, and W. Baumeister. "Perspectives of Molecular and Cellular Electron Tomography." *J. Struct. Biol.* 120 (1997), pp. 276–308.

[52] G. Möbus, R. C. Doole, and B. J. Inkson. "Spectroscopic electron tomography." *Ultramicroscopy* 96.3 (2003), pp. 433–451.

[53] M.-h. Li, Y.-q. Yang, B. Huang, X. Luo, W. Zhang, M. Han, and J.-g. Ru. "Development of advanced electron tomography in materials science based on TEM and STEM." *Trans. Nonferrous Met. Soc. China* 24.10 (2014), pp. 3031–3050.

[54] E. T. Quinto. "Artifacts and Visible Singularities in Limited Data X-Ray Tomography." *Sens Imaging* 18.9 (2017).

[55] P. A. Midgley and R. E. Dunin-Borkowski. "Electron tomography and holography in materials science." *Nat. Mater.* 8 (2009), pp. 271–280.

[56] P. Gilbert. "Iterative Methods for the 3D reconstruction of an Object from Projections." *J. Theor. Biol.* 36.1 (1972), pp. 105–117.

[57] A. C. Kak and M. Slaney. *Principles of Computerized Tomographic Imaging*. Ed. by I. Press. 1988, p. 284.

[58] R. Leary, P. A. Midgley, and J. M. Thomas. "Recent Advances in the Application of Electron Tomography to Materials Chemistry." *Acc. Chem. Res.* 45.10 (2012), pp. 1782–1791.

[59] A. Urner, M. Oblinger, V. Cauda, R. Wei, and T. Bein. "Discrete tomography of demanding samples based on a modified SIRT algorithm." *Ultramicroscopy* 115 (2012), pp. 41–49.

[60] N. Kawase, M. Kato, H. Nishioka, and H. Jinnai. "Transmission electron microtomography without the "missing wedge" for quantitative structural analysis." *Ultramicroscopy* 107 (2007), pp. 8–15.

[61] J. S. Barnard, J. Sharp, J. R. Tong, and P. A. Midgley. "Weak-beam dark-field electron tomography of dislocations in GaN." *J. Phys. Conf. Ser.* 26.247-250 (2006).

[62] W. van Aarle, W. J. Palenstijn, J. De Beenhouwer, T. Altantzis, S. Bals, K. J. Batenburg, and J. Sijbers. "The ASTRA Toolbox: A platform for advanced algorithm development in electron tomography." *Ultramicroscopy* 157 (2015), pp. 35–47.

[63] K. Kimura, S. Hata, S. Matsumura, and T. Horiuchi. "Dark-field transmission electron microscopy for a tilt series of ordering alloys: toward electron tomography." *J. Electron Microsc. (Tokyo).* 54 (2005), pp. 373–377.

[64] Z. Zhong, B. Goris, R. Schoenmakers, S. Bals, and K. J. Batenburg. "A bimodal tomographic reconstruction technique combining EDS-STEM and HAADF-STEM." *Ultramicroscopy* 174 (2017), pp. 35–45.

[65] R. Xu, C.-C. Chen, L. Wu, M. C. Scott, W. Theis, C. Ophus, M. Bartels, Y. Yang, H. Ramezani-Dakhel, M. R. Sawaya, H. Heinz, L. D. Marks, P. Ercius, and J. Miao. "Three-dimensional coordinates of individual atoms in materials revealed by electron tomography." *Nat. Mater.* 14.11 (2015), pp. 1099–1103.

[66] P. Burdet, Z. Saghi, A. N. Filippin, A. Borrás, and P. A. Midgley. "A novel 3D absorption correction method for quantitative EDX-STEM tomography." *Ultramicroscopy* 160 (2015), pp. 118–129.

[67] S. M. Collins and P. A. Midgley. "Progress and opportunities in EELS and EDS tomography." *Ultramicroscopy* 180 (2017), pp. 133–141.

[68] J. Yuan, E. Bae, X.-C. Tai, and Y. Boykov. "A Study on Continuous Max-Flow and Min-Cut Approaches." *2010 IEEE Comput. Soc. Conf. Comput. Vis. Pattern Recognit.* 2010, pp. 2217–2224.

[69] N. Volkmann. "A novel three-dimensional variant of the watershed transform for segmentation of electron density maps." *J. Struct. Biol.* 138.1-2 (Apr. 2002), pp. 123–129.

[70] W. van Aarle, W. J. Palenstijn, J. Cant, E. Janssens, F. Bleichrodt, A. Dabravolski, J. De Beenhouwer, K. J. Batenburg, and J. Sijbers. "Fast and flexible X-ray tomography using the ASTRA toolbox." *Opt. expres* 24.22 (2016), pp. 25129–2514.

[71] W. J. Palenstijn, K. J. Batenburg, and J. Sijbers. "Performance improvements for iterative electron tomography reconstruction using graphics processing units (GPUs)." *J. Struct. Biol.* 176.2 (2011), pp. 250–253.

[72] V. Migunov, H. Ryll, X. Zhuge, M. Simson, L. Strüder, K. J. Batenburg, L. Houben, and R. E. Dunin-Borkowski. "Rapid low dose electron tomography using a direct electron detection camera." *Sci. Rep.* 5 (2015).

Scientific publications

My contributions

Paper I: Electron tomography reveals the droplet covered surface structure of nanowires grown by Aerotaxy

I did all the microscopy, both HRTEM for determination of crystal structure and directions and the HAADF-STEM for the tomography. I also did the tomographic reconstructions and produced the azimuthal maps from these. I am the main author of the manuscript.

Paper II: GaAsP Nanowires Grown by Aerotaxy

I did all the TEM analysis, HRTEM imaging and compositional analysis (XEDS). I also produced the figures pertaining to these analyses.

Paper III: n-type doping and morphology of GaAs nanowires in Aerotaxy

I did all the TEM analysis, HRTEM of the wires and compositional analysis (XEDS) of the seed particles.

Appendix

Appendix A: Phase contrast transfer function calculations

The *high resolution TEM* (HRTEM) treats the electrons as a wave hitting the sample. The wave, $\Psi_{source}(\mathbf{r})$, is assumed coherent and normalized ($\Psi_{source}(\mathbf{r}) = 1$).

Starting with what is recorded in the image (i), intensity as a function of position, $I_i(\mathbf{r})$:

$$I_i(\mathbf{r}) = \mid \Psi_i(\mathbf{r}) \mid^2 = \Psi_i(\mathbf{r})\Psi_i^*(\mathbf{r}) \tag{A.1}$$

Thin enough sample (*weak phase object approximation*, WPOA): The wave exiting the object is only experiencing a slight shift in phase as a function of position, $\sigma V_t(\mathbf{r})$ (interaction factor σ and projected potential V_t):

$$\Psi_o(\mathbf{r}) = exp\big[-i\sigma V_t(\mathbf{r})\big] \approx 1 - i\sigma V_t(\mathbf{r}) \tag{A.2}$$

The total wave exiting the object is now expressed as:

$$\Psi_o(\mathbf{r}) = 1 + \Psi_{so}(\mathbf{r}), \quad \Re\Big\{\Psi_{so}(\mathbf{r})\Big\} = 0 \tag{A.3}$$

Since the interest lies in how spatial frequencies are transmitted in the microscope the Fourier transform (FT) is used to express everything in spatial frequencies $\mathbf{k}$:

$$FT\Big[\Psi_{so}(\mathbf{r})\Big] = \psi_{so}(\mathbf{k}) = -i\sigma\hat{V_t} \tag{A.4}$$

Combining equations A.1 and A.3, assuming that the wave $\Psi_i(\mathbf{r})$ at the image (i) is also composed of a unaffected direct beam (1) and a scattered component ($\Psi_{si}(\mathbf{r})$):

$$I_i(\mathbf{r}) = 1 + \Psi_{si}(\mathbf{r}) + \Psi_{si}^*(\mathbf{r}) + \mid \Psi_{si}(\mathbf{r}) \mid^2 \tag{A.5}$$

This can be further simplified by assuming the the factors containing scattered waves' interaction with other scattered waves being very small and neglecting these (called the *linear imaging approximation*):

$$I_i(\mathbf{r}) \approx 1 + \Psi_{si}(\mathbf{r}) + \Psi_{si}^*(\mathbf{r}) \tag{A.6}$$

The problem is now a linear one and can be transformed into the frequency domain:

$$FT\Big[I_i(\mathbf{r})\Big] = \mathcal{I}_i(\mathbf{k}) = \delta + \psi_{si}(\mathbf{k}) + \psi_{si}^*(\text{-}\mathbf{k}) \tag{A.7}$$

Finally, the scattered waves from the object ($\psi_{so}(\mathbf{k})$) have during their transfer to the image ($\psi_{si}(\mathbf{k})$) been subjected to non-ideal transfer due to lenses not being perfect. Factors are introduced to describe the transfer:

- $A(\mathbf{k})$, an aperture function cutting off high spatial frequencies by its position.
- $D(\mathbf{k})$, a collective term (envelope function), $D(\mathbf{k})$, that dampens higher $\mathbf{k}$ due to imperfections in the setup which can be vibrations, energy spread of incoming electrons among others.
- $exp\big[-i\chi(\mathbf{k})\big]$, a phase shift term.

By assuming functions A, D, and $\hat{V}_t$ (inserted from equation A.4) being even, this leads to:

$$\begin{aligned} \mathcal{I}_i(\mathbf{k}) &= \delta + A(\mathbf{k})D(\mathbf{k})exp\big[-i\chi(\mathbf{k})\big]\psi_{so}(\mathbf{k}) \\ &\quad + A(\text{-}\mathbf{k})D(\text{-}\mathbf{k})exp\big[-i\chi(\text{-}\mathbf{k})\big]\psi^*_{so}(\text{-}\mathbf{k}) \end{aligned} \tag{A.8}$$

$$\begin{aligned} \mathcal{I}_i(\mathbf{k}) &= \delta - i\sigma\hat{V}_t A(\mathbf{k})D(\mathbf{k})\Big(exp\big[-i\chi(\mathbf{k})\big] - exp\big[-i\chi(\text{-}\mathbf{k})\big]\Big) = \\ &= \delta - i\sigma\hat{V}_t A(\mathbf{k})D(\mathbf{k})\cdot \\ &\quad \cdot\Big(cos\big(-\chi(\mathbf{k})\big) + isin\big(-\chi(\mathbf{k})\big) - \\ &\quad - cos\big(-\chi(\text{-}\mathbf{k})\big) - isin\big(-\chi(\text{-}\mathbf{k})\big)\Big) = \\ &= \delta - i\sigma\hat{V}_t A(\mathbf{k})D(\mathbf{k})\Big(2isin\big(\chi(\mathbf{k})\big)\Big) = \\ &= \delta + 2\sigma\hat{V}_t A(\mathbf{k})D(\mathbf{k})sin\big(\chi(\mathbf{k})\big) \end{aligned} \tag{A.9}$$

The transfer of spatial frequencies to the image can be described by the three functions; $A(\mathbf{k})$, $D(\mathbf{k})$, and $sin\big(\chi(\mathbf{k})\big)$, which all depend on the setup of the microscope. [2, 37, 38]

Appendix B: Aberrations in a TEM

Table B.1: Reference table of different aberrations inlcuding their coefficient symbol, symmetry and the factor to be summed (how it scales with ω). $\bar{\omega}$ notates the conjugate of ω. Table from [39]

Aberration name	Variable	Value	Symmetry	Aberration factor
Beam/Image Shift	A_0	complex	1	$A_0\bar{\omega}$
Defocus	C_1	real	0	$\frac{1}{2}C_1\omega\bar{\omega}$
Twofold Astigmatism	A_1	complex	2	$\frac{1}{2}A_1\bar{\omega}^2$
Second-order axial coma	B_2	complex	1	$B_2\omega^2\bar{\omega}$
Threefold Astigmatism	A_2	complex	3	$\frac{1}{3}A_2\bar{\omega}^3$
Third-order spherical aberration	C_3	real	0	$\frac{1}{4}C_3(\omega\bar{\omega})^2$
Third-order star-aberration	S_3	complex	2	$S_3\omega^3\bar{\omega}$
Fourfold astigmatism	A_3	complex	4	$\frac{1}{4}A_3\bar{\omega}^4$
Fourth-order axial coma	B_4	complex	1	$B_4\omega^3\bar{\omega}^2$
Fourth-order three-lobe aberration	D_4	complex	3	$D_4\omega^4\bar{\omega}$
Fivefold astigmatism	A_4	complex	5	$\frac{1}{5}A_4\bar{\omega}^5$
Fifth-order spherical aberration	C_5	real	0	$\frac{1}{6}C_5(\omega\bar{\omega})^3$
Fifth-order star-aberration	S_5	complex	2	$S_5\omega^4\bar{\omega}^2$
Fifth-order rosette aberration	R_5	complex	4	$R_5\omega^5\bar{\omega}$
Sixfold astigmatism	A_5	complex	6	$\frac{1}{6}A_5\bar{\omega}^6$
Sixth-order axial coma	B_6	complex	1	$B_6\omega^4\bar{\omega}^3$
Sixth-order three-lobe aberration	D_6	complex	3	$D_6\omega^5\bar{\omega}^2$
Sixth-order pentacle aberration	F_6	complex	5	$F_6\omega^6\bar{\omega}$
Sevenfold astigmatism	A_6	complex	7	$\frac{1}{7}A_6\bar{\omega}^7$
Seventh-order spherical aberration	C_7	real	0	$\frac{1}{8}C_7(\omega\bar{\omega})^4$
Seventh-order star-aberration	S_7	complex	2	$S_7\omega^5\bar{\omega}^3$
Seventh-order rosette aberration	R_7	complex	4	$R_7\omega^6\bar{\omega}^2$
Seventh-order chaplet aberration	G_7	complex	4	$G_7\omega^7\bar{\omega}$
Eightfold astigmatism	A_7	complex	8	$\frac{1}{8}A_7\bar{\omega}^8$

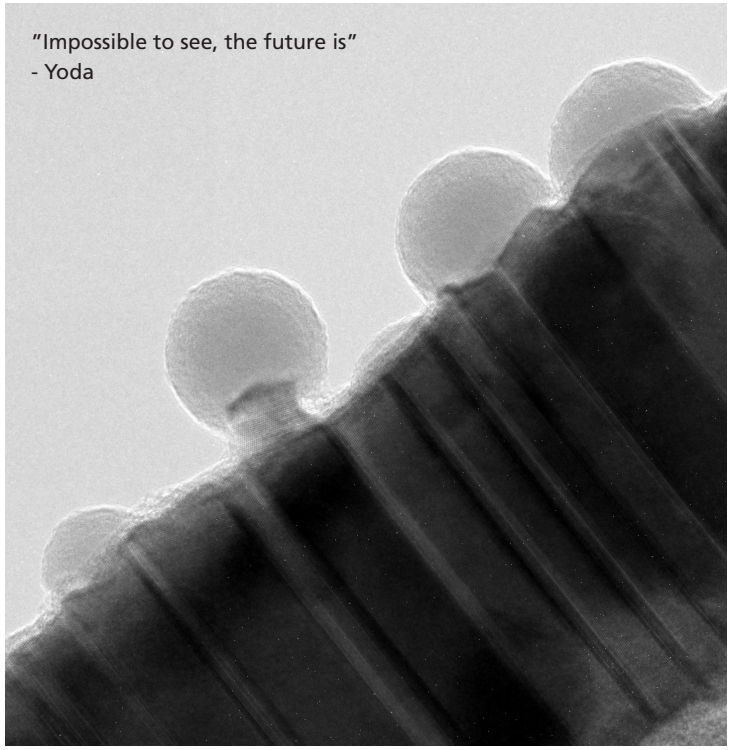

Printed by Media-Tryck, Lund 2018 NORDIC SWAN ECOLABEL 3041 0903

LUND UNIVERSITY

ISBN 978-91-7422-571-6

Centre for Analysis and Synthesis
Department of Chemistry
Faculty of Engineering
Lund University